Submillimeter Array Newsletter

Number 35, January 2023

CONTENTS

FROM THE DIRECTOR

Dear SMA Newsletter readers,

2023 promises to be an exciting and productive year for the SMA with two exciting developments:

First, as I write this the first of the wideband Submillimeter Array receiver systems has just arrived in Hilo, and will be delivered to the SMA Maunakea site tomorrow. With aging cryogenic receiver systems on all of the SMA antennas, this is an extremely welcome event. We plan to install the new receiver system into antenna #7 during the next couple of weeks, and perform extensive testing and on-sky verification of performance during the SMA shutdown next month. This new receiver package promises improved performance in a number of areas, including sensitivity, on-sky beam alignment, and reliability. A second wSMA receiver system is currently under test in the Cambridge labs, and could be shipped to Hilo towards the end of this year. While both of these systems are designated as prototypes, recent modifications that reduce the heat load of the receiver cartridges have resulted in a significant improvement in cryogenic performance, so much so that these receiver systems now fully meet the required specifications.

Second, last Fall CfA Director Lisa Kewley initiated a call to scientific or technical staff to submit proposals to inform strategic planning at the CfA. Over sixty proposals were received, more than a quarter of which supported SMA science initiatives or technical advances in SAO's Submillimeter Receiver Laboratory. In order to evaluate these proposals in terms of a coordinated long range vision for the observatory, a two-day retreat for CfA scientific and engineering staff has been organized for the end of February.

Watch this space, and have a great observing season.

Raymond Blundell

ACCRETION BURST ECHOES AS PROBES OF PROTOSTELLAR ENVIRONMENTS AND EPISODIC MASS ASSEMBLY

Logan Francis[1,2], Doug Johnstone[1,2], Jeong-Eun Lee[3,4], Gregory J. Herczeg[5,6], Feng Long[7], Steve Mairs[8,9], Carlos Contreras Peña[4], and Gerald Moriarty-Schieven[2], The JCMT Transient Team

Protostars in the youngest stages of evolution grow via the infall of material from their surrounding envelopes to a circumstellar disk, followed by stellar accretion channeled through the disk. The stellar accretion rate is expected to be highly variable owing to a wide range of possible disk instabilities and perturbations (see Fischer et al. (2022) for a recent review). Most of a protostar's final mass ($\gtrsim 90\%$) is incorporated during the embedded phase (Fischer et al. 2022), a large fraction (~25%) of which may accreted in short outbursts (Mckee and Offner 2011, Fischer et al. 2019). Observational measurements of the frequency and amplitude of accretion outbursts are thus of fundamental importance for star formation theory. The clumpy structure of outflows, (e.g., Plunkett et al. 2015; Jhan et al. 2022) effects of past outbursts on envelope chemistry (e.g., Jørgensen et al. 2013), and the detection of a handful of bright outbursts from mid-IR to mm wavelengths (e.g. Safron et al. 2015, Hunter et al. 2017) all suggest that outbursts occur often in the embedded stage. However, the deeply embedded nature of the youngest protstars precludes conventional measurements of the accretion rate, such as the UV continuum excess or Hα emission line strength (Hartmann et al. 2016), necessitating alternative methods for quantifying accretion variability.

Radiative transfer modeling of the envelope response to accretion outbursts has shown that changes in the accretion rate can produce an observable far-IR to mm response in the envelope dust continuum emission (Johnstone et al. 2013, MacFarlane et al. 2019a, 2019b). In the far-IR, the change in observed brightness is approximately proportional to the change in luminosity, while at (sub)mm wavelengths, the brightness change instead traces variations in the envelope temperature (Contreras Peña et al. 2020). Using this strategy, the ongoing James Clerk Maxwell Telescope (JCMT) Transient Survey (Herczeg et al. 2017) thus searches for changes in dust emission due to accretion variability by monitoring several nearby star forming regions at 450 and 850 μm. In the first 4 yr of Transient Survey observations, 18 of 83 class 0 and I protostars have been found to exhibit moderate secular variability on timescales of a few years, though the estimated mass accreted during these variations was at most a few percent of the stellar mass (Lee et al. 2021).

Although the Transient Survey monitors a large number of protostars, the typical resolution at 850 μm is only 15.6", or a few 1000 au at the distance to most nearby star forming regions. The modeling work of Johnstone et al. (2013) suggests that heating by the interstellar radiation field (ISRF) may dominate the emission from the outer envelope traced by such low resolution observations. Higher resolution surveys may therefore be more sensitive to changes in the accretion rate. We thus obtained SMA observations of the class I protostar EC 53 (V371 Ser), a known ~18 month periodic variable (Yoo et al. 2017) in the Serpens star forming region (distance: 436 pc, Ortiz-León et al. (2017); Herczeg et al. (2019)). The SMA data were taken from 2021-02-19 to 2021-09-21 during the most recent outburst of EC 53, and complement 850 μm Transient Survey observations covering the same period. The SMA was used in either the compact or subcompact configurations to provide a typical beam

[1] Department of Physics and Astronomy, University of Victoria; [2] NRC Herzberg Astronomy and Astrophysics; [3] School of Space Research, Kyung Hee University; [4] Department of Physics and Astronomy, Seoul National University; [5] Kavli Institute for Astronomy and Astrophysics, Peking University; [6] Department of Astronomy, Peking University; [7] Center for Astrophysics, Harvard & Smithsonian; [8] SOFIA Science Center, Universities Space Research Association, NASA Ames Research Center; [9] East Asian Observatory
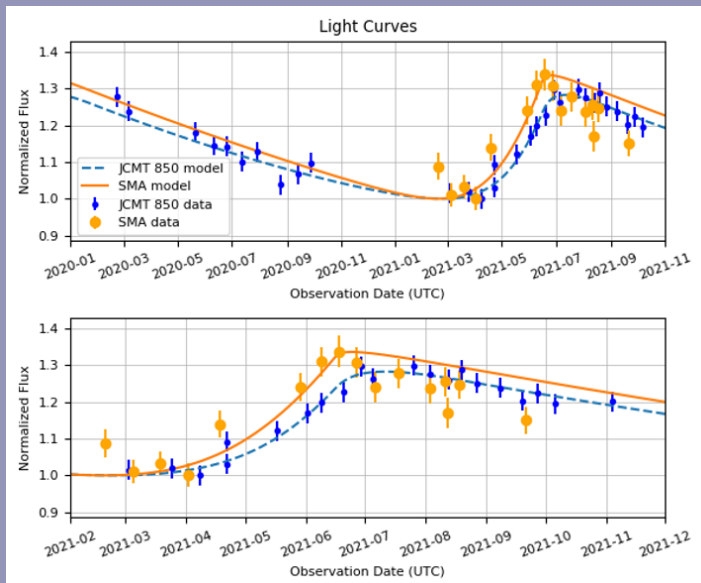
Figure 1: Comparison of our fiducial EC 53 model light curves and the observations from the SMA and JCMT (850 μm). The models and observations are shown over the 2020 decay and 2021 outburst (top), and zoom in on the 2021 outburst (bottom). The model light curves are normalized to the minimum flux, while the data are normalized to the minimum observed flux of EC 53 on 2021 April 2 for the SMA and 2021 April 8 for the JCMT.

size of 3″. The 230/240 GHz RxA/RxB pair was used for all observations and tuned to LO frequencies between 238.5 ± 10.0 GHz. Our SMA observations also targeted 3 additional stable young stellar objects, which we use as additional calibration sources to obtain a relative flux scale accuracy of 3% epoch-to-epoch. A similar flux calibration scheme is used by the Transient Survey to obtain a relative calibration accuracy of ~1% (Mairs et al. 2017).

The final calibrated light curves of EC 53 from the SMA and JCMT are shown in **Figure 1**. To compare the relative amplitudes of the light curves, we normalize the flux at each light curve to the lowest pre-outburst fluxes in April 2021. The light curve of EC 53 is observed to peak several weeks earlier, and is somewhat stronger in the SMA observations, with an amplitude change of ~35% vs ~30% at the JCMT. The observed delay and amplitude difference between the SMA and JCMT light curves suggests that resolution of the observations, and therefore the spatial scale of the envelope, plays an important role in modulating the dust response to an increase in accretion luminosity.

To interpret the observed light curves, we develop a simple toy model for the EC 53 envelope's response to an accretion outburst. Motivated by an envelope model previously derived from fits to the spectral energy distribution of EC 53 by Baek et al. (2020), we consider a 10,000 au radius envelope with spherical symmetry and power law density and temperature profiles. A minimum floor temperature T_{floor} is included in the temperature profile to approximate the effect of external heating by the ISRF. We use a periodic luminosity function with exponential rise and fall timescales of 35 and 270 days respectively, the values of which were derived by empirical fits to the mid-IR light curve of EC 53 over several outburst

cycles (Lee et al. 2020). In previous radiative transfer modeling of the envelope response to a burst, Johnstone et al. (2013) found that the dust heating time is negligible, so we assume this timescale to be zero. Furthermore, we do not consider the details of the dust opacity, and assume the observed emission from the envelope is optically thin.

The finite light travel time through the envelope is important, as it can impose a time delay of weeks to months on the observed brightening of the dust emission. In **Figure 2**, contours of the lookback time, $t_{lb} = (\sqrt{x^2 + z^2} - x)/c$, are shown overlaid on our model envelope with the physical scales of the SMA and JCMT beams indicated, where $t_{lb} = 0$ days corresponds to the
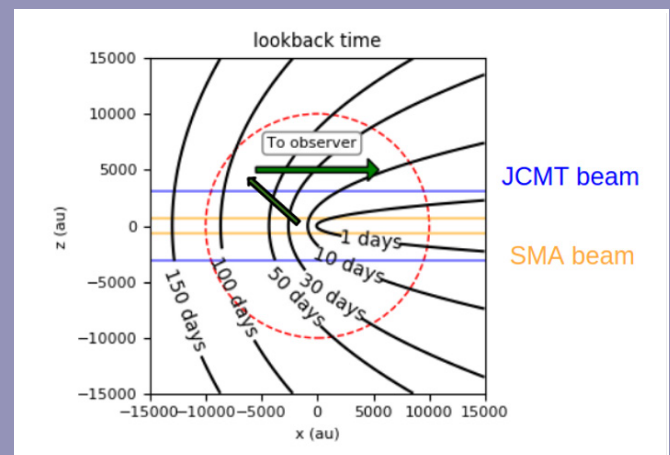
Figure 2: Lookback time contours over the domain used for our toy model envelope. The dashed red circle denotes the outer envelope edge, while the solid blue and orange lines show the radii of our model beams for JCMT 850 μm (3270 au) and SMA (654 au).
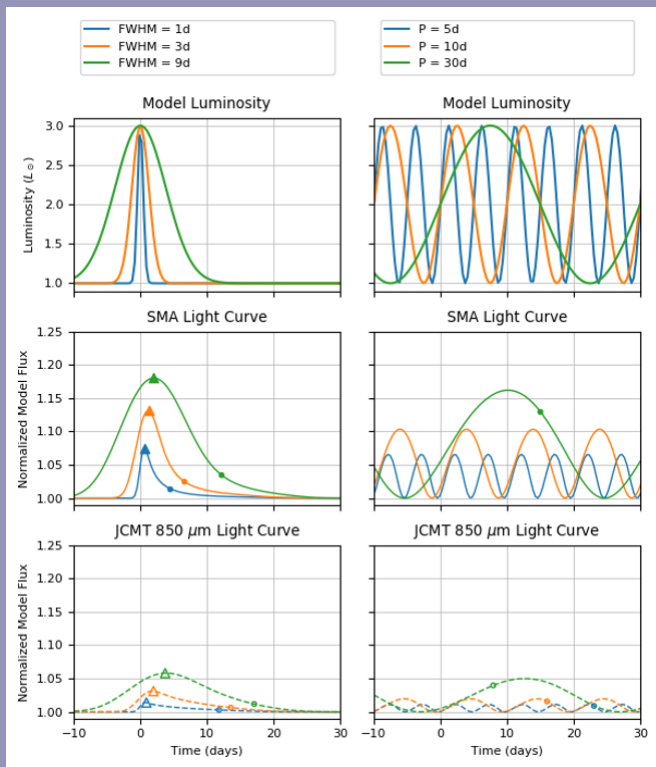
Figure 3: Comparison of the responses of the fiducial EC 53 envelope model to Gaussian (left column), and sine wave (right column) luminosity functions with various shapes. Top row: input luminosity function; middle row: normalized model SMA light curve; bottom row: normalized model JCMT light curve. For the Gaussian model, the maximum flux and the time during the decay when 20% of the maximum flux is reached are shown by the triangles and circles, respectively.

on the observed data in **Figure 2**. We find that a floor temperature of ~24K is important to include, as it plays the largest role in determining the difference in amplitude between the model SMA and JCMT light curves. Overall, our model is a good match to the earlier rise and stronger amplitude seen in the SMA light curve, however, the observed decay is quicker in the SMA observations. Near infrared observations of EC53 show additional structure around the burst peak, suggesting the change in luminosity may be more complex than in our toy model.

To explore the effect of the envelope in modulating the observed light curve, we also produce model light curves using Gaussian and sine wave luminosity functions propagating through our fiducial EC 53 envelope model. For Gaussian luminosity functions (left column of **Figure 3**), the lag timescale for the observed light curve to return from the peak flux (triangles) to the 20% level (circles) is significantly shorter, 17-21 days for the JCMT in comparison to 4-9 days for the SMA. In the case of sine wave luminosity variations, this longer lag timescale results in a greater reduction in the light curve amplitude at the JCMT than the SMA, which is particularly pronounced for the shortest 5 day period variations. It is therefore plausible that rapid, <30 day variations in luminosity near the light curve peak may be responsible for the quicker decline in the SMA observations.

Our work demonstrates the possibility of robustly measuring variability from embedded protostars with sub-mm/mm interferometry. This is enabled by our relative flux calibration scheme, which delivers an unprecedented 3% accuracy, compared to the typical absolute flux calibration accuracy of 10-15% for sub-mm/mm observations. Our toy model shows that the detected time lag and amplitude difference between the JCMT and SMA light curves in the 2021 outburst of EC 53 is plausibly explained by the time delay from the light travel time and inclusion of additional colder, ISRF influenced envelope material within the JCMT beam. Further details on our relative flux calibration strategy, the variability of other embedded protostars observed in a companion program with ALMA, and a detailed exploration of how the physical parameters of the envelope and observational properties affect the model light curve may be found in the corresponding journal article (Francis et al. 2022).

time when photons first reach the observer. The larger beam of the JCMT implies that it sees much more envelope material at larger radii, colder temperatures, and longer lookback times than the SMA.

We fit our normalized model light curves to the observations by varying the floor temperature, ratio of minimum to maximum luminosity, period, and the date of peak luminosity . Our best-fitting model light curves (solid orange and blue lines) with the flux scaled to pre-burst minimum value are overlaid

REFERENCES

- Contreras Peña, C., Johnstone, D., Baek, G., et al. 2020, MNRAS, 495, 3614
- Fischer, W., Dunham, M., Green, J., et al. 2019, BAAS, 51, 495
- Fischer, W. J., Hillenbrand, L. A., Herczeg, G. J., et al. 2022, arXiv:2203. 11257
- Francis, L, Johnstone, D., Lee, J., et al. 2022, ApJ, 937, 29
- Hartmann, L., Herczeg, G., & Calvet, N. 2016, ARA&A, 54, 135
- Herczeg, G. J., Johnstone, D., Mairs, S., et al. 2017, ApJ, 849, 43
- Herczeg, G. J., Kuhn, M. A., Zhou, X., et al. 2019, ApJ, 878, 111
- Hunter, T. R., Brogan, C. L., MacLeod, G., et al. 2017, ApJL, 837, L29
- Jhan, K.-S., Lee, C.-F., Johnstone, D., et al. 2022, ApJL, 931, L5
- Johnstone, D., Hendricks, B., Herczeg, G. J., & Bruderer, S. 2013, ApJ, 765, 133
- Jørgensen, J. K., Visser, R., Sakai, N., et al. 2013, ApJL, 779, L22

- Lee, Y.-H., Johnstone, D., Lee, J.-E., et al. 2020, ApJ, 903, 5
- Lee, Y.-H., Johnstone, D., Lee, J.-E., et al. 2021, ApJ, 920, 119
- MacFarlane, B., Stamatellos, D., Johnstone, D., et al. 2019a, MNRAS, 487, 4465
- MacFarlane, B., Stamatellos, D., Johnstone, D., et al. 2019b, MNRAS, 487, 5106
- Mairs, S., Lane, J., Johnstone, D., et al. 2017, ApJ, 843, 55
- McKee, C. F., & Offner, S. R. R. 2011, in Proc. IAU 270, Computational Star Formation,
- ed. J. Alves et al. (Cambridge: Cambridge Univ. Press), 73
- Ortiz-León, G. N., Dzib, S. A., Kounkel, M. A., et al. 2017, ApJ, 834, 143
- Plunkett, A. L., Arce, H. G., Mardones, D., et al. 2015, Natur, 527, 70
- Safron, E. J., Fischer, W. J., Megeath, S. T., et al. 2015, ApJL, 800, L5
- Yoo, H., Lee, J.-E., Mairs, S., et al. 2017, ApJ, 849, 69

EFFECTS OF MAGNETIC FIELD ORIENTATIONS IN DENSE CORES ON GAS KINEMATICS IN PROTOSTELLAR ENVELOPES

Aashish Gupta[1,2,3], Hsi-Wei Yen[2], Patrick Koch[2], Pierre Bastien[4], Tyler L. Bourke[5,6], Eun Jung Chung[7], Tetsuo Hasegawa[8], Charles L. H. Hull[9,10], Shu-ichiro Inutsuka[11], Jungmi Kwon[12], Woojin Kwon[13,14], Shih-Ping Lai[2,15], Chang Won Lee[16,17], Chin-Fei Lee[2], Kate Pattle[18], Keping Qiu[19,20], Mehrnoosh Tahani[21], Motohide Tamura[12,22,23], and Derek Ward-Thompson[24]

Protostellar disks play a crucial role in both star and planet formation but details of how these disks form remain unclear. Traditionally, disk formation was understood as a simple consequence of angular momentum conservation (Bodenheimer 1995). However, the picture becomes more complicated when the magnetic field is considered. Ideal MHD simulations have shown that realistic levels of magnetic field strengths can transport a significant amount of angular momentum outward and greatly suppress the formation of disks (Mellon & Li 2008), which is in tension with observations of Keplerian disks around young protostars. This is often referred to as the 'magnetic braking catastrophe'. Simulations of collapsing dense cores have suggested that including the misalignment between the rotational axis and the magnetic field can reduce the efficiency of magnetic braking and thus be a possible solution to this catastrophe (Joos et al. 2012; Li et al. 2013).

Observationally, the role of this misalignment on angular momentum transfer is not yet well understood. For a sample of ~20 protostars, Galametz et al. (2020) compared the misalignments between the magnetic fields in the protostellar envelopes and the outflow axes with the magnitudes of the velocity gradients in the envelopes, where the outflow axes were adopted as a proxy for the rotational axes of the protostellar sources. They found a positive correlation between the misalignment and the velocity gradient, which would suggest that a larger misalignment reduces the efficiency of magnetic braking. On the other hand, Yen et al. (2021) compared the sizes and fluxes of a sample of ~50 protostellar disks with the misalignment between their rotational axes and core-scale magnetic fields and found no significant correlation. This would suggest that misalignment does not play a crucial role in disk formation.

In order to investigate how dynamically important misalignment between the magnetic field and rotational axis in a dense core is in the star formation process, we studied ~1,000 au envelope-scale kinematics in synergy with ~4,000 au core-scale magnetic field orientations, for a sample of 32 Class 0 and I protostars in the Perseus cloud in our recent publication.

[1] Graduate Institute of Astronomy, National Central University; [2] Academia Sinica Institute of Astronomy and Astrophysics; [3] European Southern Observatory; [4] Centre de recherche en astrophysique du Québec & département de physique, Université de Montréal; [5] SKA Observatory, [6] Center for Astrophysics I Harvard & Smithsonian; [7] Department of Astronomy and Space Science, Chungnam National University; [8] National Astronomical Observatory of Japan, Japan; [9] National Astronomical Observatory of Japan, Chile; [10] Joint ALMA Observatory; [11] Department of Physics, Nagoya University; [12] Department of Astronomy, University of Tokyo; [13] Department of Earth Science Education, Seoul National University; [14] SNU Astronomy Research Center, Seoul National University; [15] Institute of Astronomy and Department of Physics, National Tsing Hua University; [16] Korea Astronomy and Space Science Institute; [17] University of Science and Technology; [18] Department of Physics and Astronomy, University College London; [19] School of Astronomy and Space Science, Nanjing University; [20] Key Laboratory of Modern Astronomy and Astrophysics, Nanjing University; [21] Dominion Radio Astrophysical Observatory, Herzberg Astronomy and Astrophysics Research Centre; [22] Astrobiology Center; [23] National Astronomical Observatory; [24] Jeremiah Horrocks Institute, University of Central Lancashire
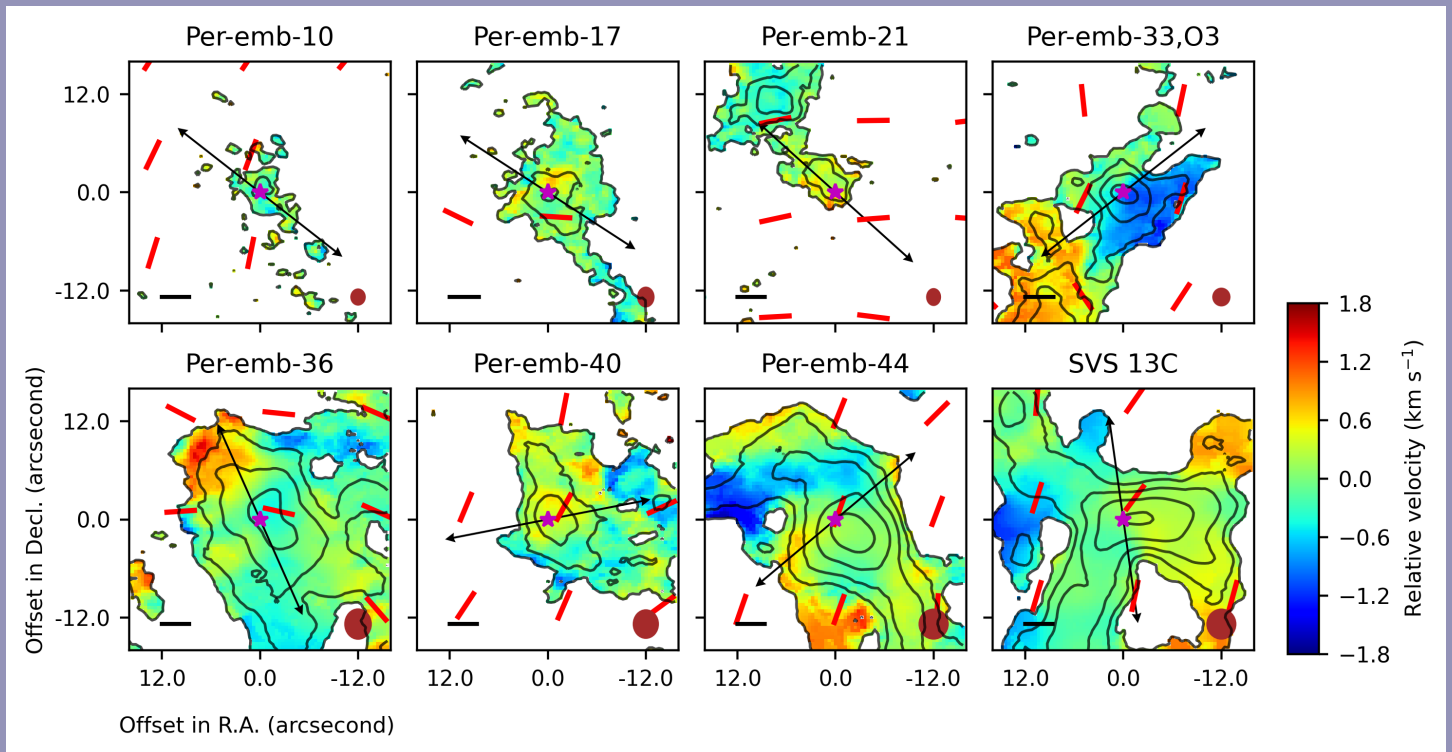
Figure 1: Magnetic field orientations observed with JCMT (red segments) overlaid on the $C^{18}O$ moment 1 (color) and 0 (contours) maps obtained with the SMA observations. Purple stars represent locations of the protostars and black arrows originating from them show outflow orientations. Black segments in the bottom-left corners depict a length scale of 1,000 au. Brown ellipses in the bottom-right corners depict beam sizes of the $C^{18}O$ data. In each panel, the outermost contour represents the 3σ noise level in the moment 0 map and subsequent inner contours levels are increasing by a factor of two.
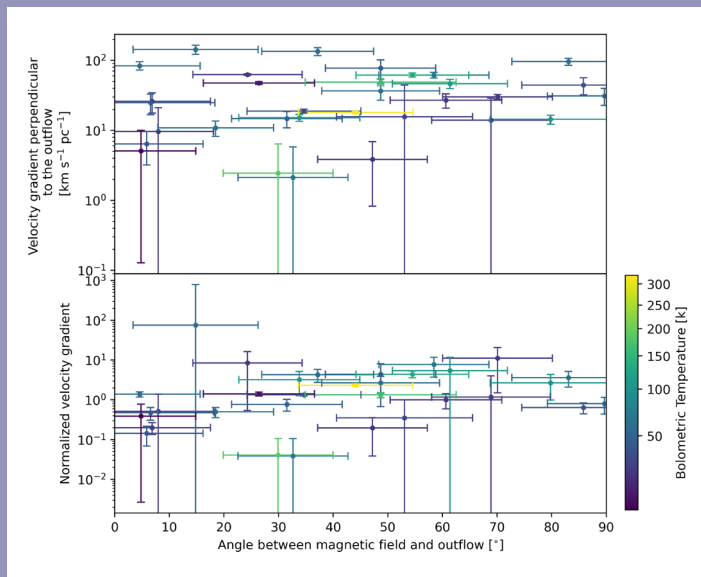
In this study, the gas kinematics were analyzed using $C^{18}O$ (2-1) data at a resolution of ~600 au taken by the Mass Assembly of Stellar Systems and their Evolution with the Submillimeter Array (SMA) survey (MASSES; Stephens et al. 2019). The MASSES survey also measured outflow orientations in a subset of their sample (Stephens et al. 2017), which can be taken as a proxy for the rotational axes of these systems. Intensity-weighted mean velocity (moment 1) maps for $C^{18}O$ data cubes are shown in Fig. 1. To quantify the gas kinematics in the protostellar envelopes, we fit these velocity structures to get three different velocity gradients, namely (1) an overall velocity gradient, which traces overall envelope-scale kinematics, (2) a velocity gradient perpendicular to the outflow, which is expected to be proportional to the rotational motion and (3) a velocity gradient parallel to the outflow, which is expected to be proportional to the infalling motion. In addition, we also computed normalized rotational gradients by dividing the rotational gradients by the infalling gradients. In this Newsletter, we focus on the key results obtained using rotational gradients and normalized rotational gradients.

In order to measure magnetic field structures in the dense cores, we used the JCMT polarimetric data at 850 μm in the Perseus molecular cloud. The data were obtained with the POL-2 polarimeter as part of the large program survey BIS-TRO (Ward-Thompson et al. 2017) and the regular projects (M17AP073 and M17BP058; PI: W. Kwon). Using the magnetic field structures (shown as red segments in Fig. 1), we measured core-scale (~4,000 au) field orientations and angular dispersions. We computed angles between core-scale field orientations and outflows, and then compared these misalignment angles to envelope-scale velocity gradients.

Figure 2 shows the rotational and normalized rotational gradients in the protostellar envelopes as a function of the misalignment. The Spearman correlation coefficients and corresponding p-values are 0.22 and 0.23 for the rotational gradient and 0.35 and 0.05 for the normalized rotational gradient. The coefficient and p-value for the rotational gradients suggest that the angular momentum in the protostellar envelopes does not strongly depend on the misalignment. In contrast to that, with a p-value of 0.05, the normalized rotational gradient likely has a significant dependence on the magnetic
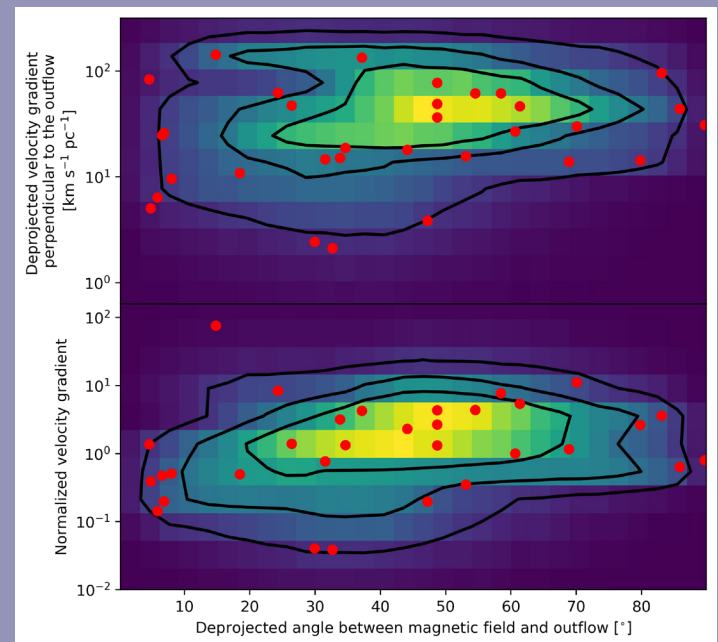
field orientation. This can also be seen in **Figure 2**, where unlike the rotational gradients (top panel), the normalized rotational gradient (bottom panel) shows an increase from ≲1 for the projected magnetic fields roughly parallel to the outflow axes to ≳1 for nearly orthogonal configurations.

However, this simple correlation coefficient analysis does not account for uncertainties in the measurements of both the velocity gradients and the misalignment angles. Moreover, the angles measured between the outflows and the magnetic field orientations are angles projected on the plane of the sky (POS), and the actual misalignment in three-dimensional (3D) space might differ significantly. As derived in Appendix C of our paper, for a given projected angle, the actual angle in 3D space can be determined if the inclinations of the magnetic field and the outflow relative to POS are known. However, since the 3D orientations of the magnetic fields and the outflows in our sample are not known, we assumed a cosine distribution of these angles and estimated the underlying probability distribution of the deprojected misalignment angles.

Accounting for the measurement and projection uncertainties, we simulated expected probability distributions of velocity gradients and misalignment angles from our observational measurements, as shown in **Figure 3**. Quantitatively, the correlation coefficient analysis is not straightforward for these simulated distributions as the number of data points is artificially too large and thus, p-values estimated using the standard methods will come out to be too small. Instead, we generated groups of 32 simulated data points, where for each group we randomly picked one simulated data point corresponding to one source in our sample of 32 sources. For each of these groups, we then calculated Spearman correlation coefficients. The resulting mean values of these correlation coefficients, taken as the representative values of our simulated distributions, are 0.14 for the rotational gradient and 0.22 for the normalized gradient. To test the significance of these correlations, we generated artificial uncorrelated samples and obtained again the distributions of their correlation coefficients. We found that for the random data, the probability to obtain correlation coefficients greater than or equal to the mean correlation coefficients are 0.22 for the rotational gradient and 0.12 for

Figure 2: Misalignment between the magnetic field and outflow axis in dense cores as a function of velocity gradient perpendicular to the outflow (top panel) and velocity gradient perpendicular to the outflow divided by that along the outflow axis (bottom panel) in the protostellar envelopes at a 1,000 au scale. Marker colours represent bolometric temperatures of corresponding protostars.

Figure 3: Simulated probability distributions of deprojected rotational gradient (top panel) and normalized rotational gradient (bottom panel) in the protostellar envelopes with respect to deprojected misalignment angles between the core-scale magnetic fields and outflow axes. Red circles represent the original measurements. Contours represent probability levels: 0.89, 0.61, 0.38 for the top panel and 0.86, 0.60, 0.27 for the bottom panel.

the normalized gradient. This suggests that the normalized rotational gradient is possibly correlated with the misalignment at a confidence level of 88%.

To conclude, we do not find any strong dependence of rotational gradients on misalignment angles. However, we infer a much stronger dependence if we normalize the rotational gradients by their infalling velocity gradients. Assuming that the infalling velocity is proportional to the mass of a central

protostar-disk system, our results could suggest that for similar central masses, more angular momentum is transported to protostellar envelopes in systems with a greater misalignment. This hints that misalignment between the magnetic field and rotational axis in a dense core can promote angular momentum transport from large to small scales, although it is unlikely a dominant factor.

REFERENCES

- Bodenheimer, P. 1995, ARA&A, 33, 199
- Mellon, R. R., & Li, Z.-Y. 2008, ApJ, 681, 1356
- Joos, M., Hennebelle, P., & Ciardi, A. 2012, A&A, 543, A128
- Li, Z.-Y., Krasnopolsky, R., & Shang, H. 2013, ApJ, 774, 82
- Galametz, M., Maury, A., Girart, J. M., et al. 2020, A&A, 644, A47

- Yen, H.-W., Zhao, B., Koch, P. M., & Gupta, A. 2021, ApJ, 916, 97
- Stephens, I. W., Bourke, T. L., Dunham, M. M., et al. 2019, ApJS, 245, 21
- Stephens, I. W., Dunham, M. M., Myers, P. C., et al. 2017, ApJ, 846, 16
- Ward-Thompson, D., Pattle, K., Bastien, P., et al. 2017, ApJ, 842, 66

VIRIAL CLUMPS IN CENTRAL MOLECULAR ZONE CLOUDS

Philip C. Myers[1], H. Perry Hatchfield[2], & Cara Battersby[1,2]

1. Introduction

1.1 Star Formation in the CMZ

The Central Molecular Zone (CMZ) in the central ~250 pc of the MIlky Way (MW), has physical properties similar to those of high-redshift galaxies (Kruijssen & Longmore 2013). At a distance from the Sun of only 8.2 kpc it is close enough to study star-forming gas with much finer resolution than in any other galactic nucleus. The CMZ has a rich history of star formation, harboring massive star clusters with ages of 2-6 Myr, including the Nuclear, Arches, and Quintuplet clusters.

Despite this history, the present-day star formation rate (SFR) of the CMZ is lower by an order of magnitude than expected from its prevalence of gas denser than $\sim 10^4$ cm^{-3}, the typical density of star-forming gas in much of the MW (Mills et al. 2018, Lada et al. 2012, Longmore et al. 2013).

It has been suggested that the SFR in the CMZ may be suppressed by its relatively high level of turbulent pressure (Rathborne et al. 2014, Federrath et al. 2016). In more than 40 barred galaxies, nuclear gas on 150 pc scales has significantly greater velocity dispersion, turbulent pressure, and virial parameter than in galaxy disks or than in nuclei of unbarred galaxies (Sun et al. 2020). These turbulent motions may unbind or disperse clumps before they can fragment and collapse to form protostellar clusters. Candidate drivers of CMZ turbulence include gas flows, star formation feedback, tidal forces and orbital dynamics (Krumholz et al. 2017, Kruijssen et al. 2019). For a recent review, see Bryant & Krabbe (2021).

1.2. This paper

This Science Highlight is a summary of Myers et al. 2022 (hereafter MHB22). This paper addresses the question of CMZ star formation by analyzing the first unbiased and complete survey of high column density gas in the CMZ on 0.1 pc scales in the submillimeter. These SMA observations resolved more than 700 clumps having column density $N>10^{22}$ cm^{-2} (CMZoom: Battersby et al. 2020; Hatchfield et al. 2020, hereafter H20). A Science Highlight describing observational results from H20 appeared in *SMA Newsletter 31* (January 2021). MBH22 analyzed the SMA observations reported in H20 with models of virial equilibrium and stopped accretion. These analyses indicate that most CMZ clumps are gravitationally unbound and either pressure-confined or transient. Their typical clump mass distribution (CMD) has a high-mass power-law slope ≈-1. This slope indicates that the time scale of clump accretion stopping is similar to its time scale of accretion, of order 0.1 Myr. Together these results suggest that star formation in CMZ clumps is suppressed because the clumps cannot gravitationally bind their turbulent motions, and because they are likely to stop accreting before they can significantly increase their mass.

2. Virial Analysis in the log N – log M Plane

The clumps observed in H20 are analyzed with a model of pressure-bounded virial equilibrium (PVE) of a uniform, self-gravitating magnetized sphere with random internal motions in a medium of uniform external pressure (Spitzer 1978, Field et al. 2011). In its standard application, PVE is analyzed in a plot of log σ^2/R vs. log N where σ is the clump velocity dispersion and R is its radius. However only a fraction ~0.1 of the ~700 clumps detected in the continuum observations of H20 were also detected in spectral line emission with enough sensitivity to be used for standard PVE analysis (Callanan et al. 2022). Therefore we used an alternate form of PVE analysis ("N – M PVE"), where the variables are clump column density N and mass M, and where the velocity dispersion σ is a parameter.

[1] Center for Astrophysics | Harvard & Smithsonian; [2] University of Connecticut, Department of Physics
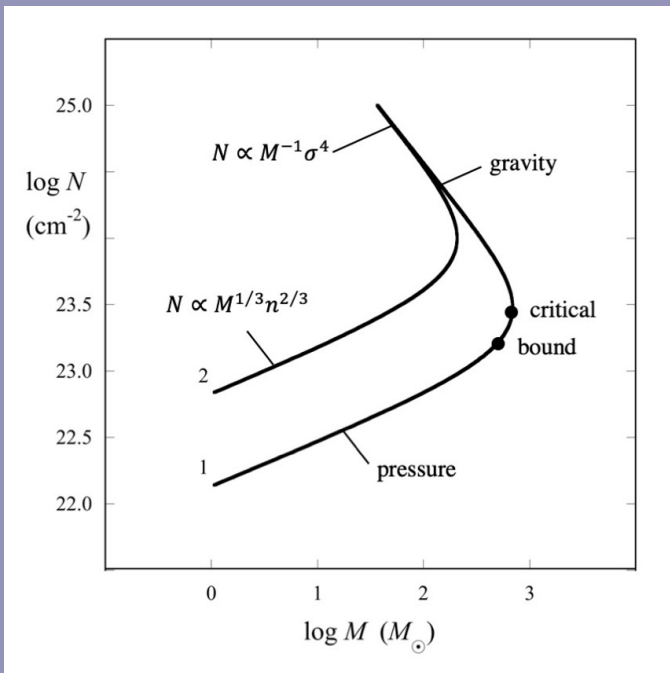
Figure 1: Pressure-bounded virial equilibrium (PVE) models in N − M form for a uniform sphere in a medium of constant external pressure P_S, for two values of P_S. In each case the velocity dispersion is σ=2 km s^{-1} and the magnetic field strength is negligible. Curve 1 has pressure P_S/k=1.0×10^8 cm^{-3} K, where k is Boltzmann's constant. Its "critical" point has column density N_0=3×10^{23} cm^{-2}. Curve 2 has P_S/k=9.2×10^8 cm^{-3} K and N_0=1×10^{24} cm^{-2}. For each curve, the "bound" point marks the transition between the pressure-bound and gravity-bound branches, where the virial and magnetic parameters have the ratio α/c_M =2. Each curve is labelled with the limiting power-law dependence of N on M. In the pressure-bound limit, $N \propto M^{1/3}$, and in the gravity-bound limit, $N \propto M^{-1}$.
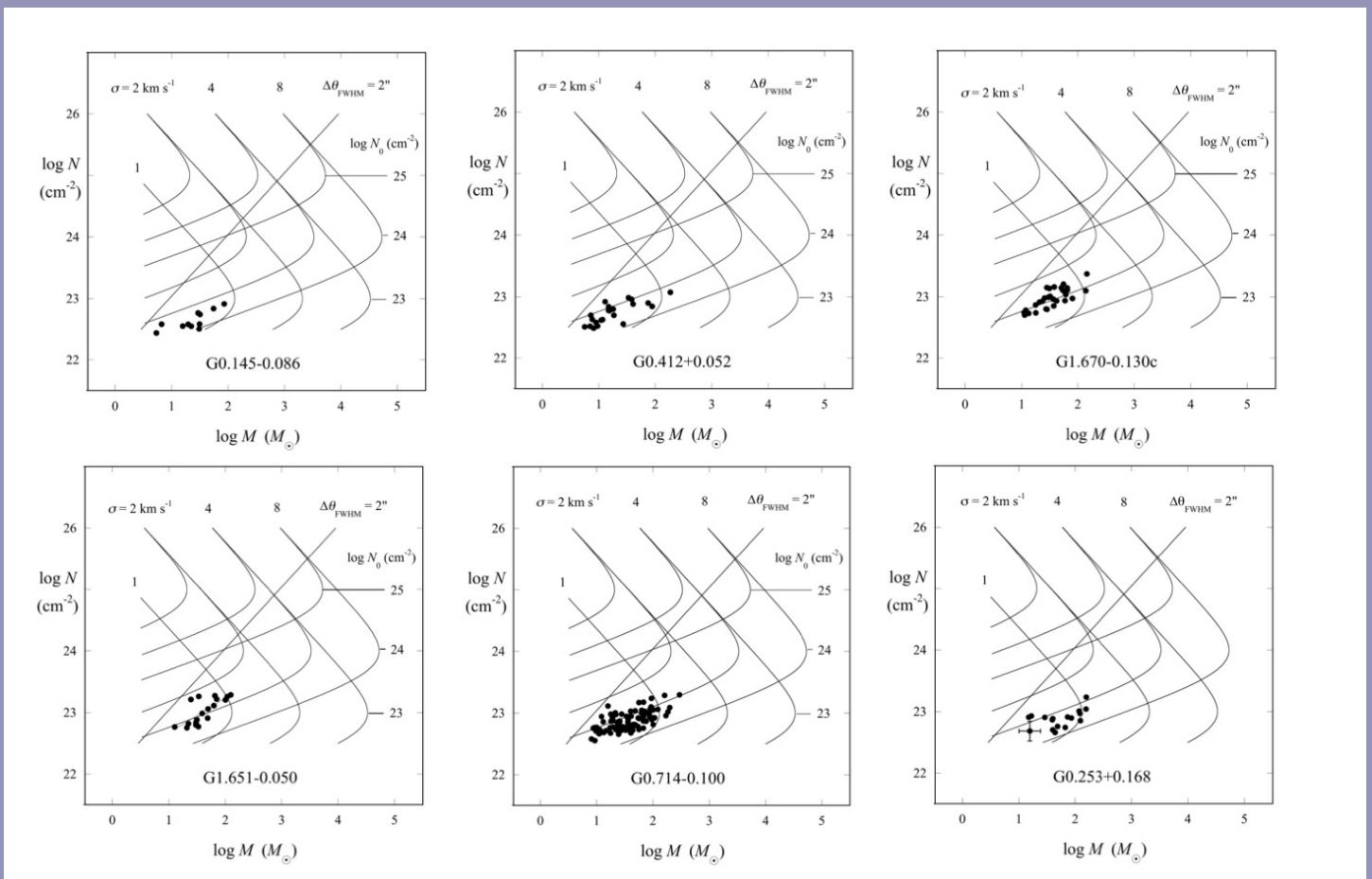
Figure 2: log-log plots of N *vs.* M for six of the 24 CMZ clouds having low-mass clumps, superposed on PVE curves as in Figure 1. In each cloud the data points approximate a linear trend with slope $s \gtrsim 1/3$, coinciding with the pressure-bound branch of a PVE curve. The line of slope 1 indicates the trend for marginally resolved clumps, whose diameter equals the beam diameter.
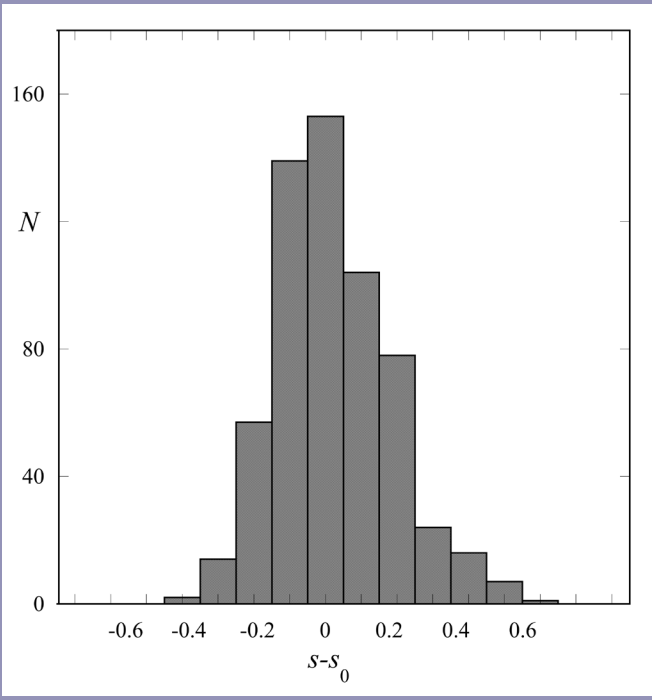
Figure 3: Distribution of log-log "clump slopes" s for the 595 clumps in CMZ sample, after exclusion of high-mass outliers. Each clump slope is the slope of a line from the clump point (log N,log M) to the intercept a of the best-fit slope line log $N=a+b$ log M for its cloud, at (a,0). The display is centered on the reference value s_0=0.38.

Figure 1 shows two $N-M$ PVE curves with different external pressure P_S. It shows that clumps with constant P_S and negligible self-gravity follow the trend $N \propto M^s, s \gtrsim s_p$=1/3. Here s_p is the exponent of M in the pressure-bound limit of PVE. Such clumps lie along the pressure-bound branch of a $N-M$ PVE curve, if they have similar external pressure and similar velocity dispersion. This property $N \propto M^s, s \gtrsim s_p$=1/3. is prevalent among CMZ clumps in nearly all CMZ clouds. Thus assessment of clump binding with $N-M$ PVE is a useful alternative to standard PVE for clouds which have a low fraction of observed velocity dispersions and a high fraction of gravitationally unbound clumps.

For all 24 CMZ clouds in H20 Table 5 having at least 10 dendrogram leaves, log N − log M diagrams were compiled, and PVE templates similar to those in **Figure 1** were superposed. **Figure 2** shows such log N − log M diagrams for six CMZ clouds having relatively low-mass clumps. Their clumps illustrate the trend $N \propto M^s, s \gtrsim s_p$=1/3, consistent with pressure-bound PVE as described above. For some of the clouds having more massive clumps, one or two clumps are outliers from the masses and slopes of their lower-mass counterparts.

To quantify the log N − log M slopes in the entire CMZ sample, **Figure 3** shows a distribution of log N − log M slopes for 595 clumps, excluding high-mass outliers. This distribution of slopes has mean ± standard error = 0.38 ± 0.01 and median 0.36. This value is consistent with clumps whose slope is slightly greater than the PVE limit of s_p=1/3=0.33.

The trend $N \propto M^s, s \gtrsim s_p$=1/3 in **Figures 2 and 3** cannot be due to poorly resolved clumps, since those clumps would follow $N \propto M^1$. It cannot be due to clumps detected at the sensitivity limit, since then $N \propto M^0$. It cannot be due to clumps which are strongly gravitationally bound, since then $N \propto M^{-1}$.

For clouds having clumps more massive than in **Figure 2**, some clumps depart from the above trend $N \propto M^s, s \gtrsim s_p$=1/3. Nine of these clouds have one or two such clumps, whose mass exceeds the typical clump mass by a factor ~10 and whose column density lies above the $s \approx 1/3$ trend line by a factor of ~3. These outlier clumps have positions which appear close to that of critical binding in **Figure 1**. All nine CMZ clouds with such outlier clumps were fit with a PVE model, assuming that most massive outlier clump is critically bound. These data and their fits are shown in **Figure 4**.

The histogram in **Figure 3** and the PVE model fits in **Figure 4** indicate that many CMZ clouds are consistent with clumps in PVE in a turbulent pressure environment. The fits also indicate that only about 5% of the clumps are gravitationally bound with virial parameter α<2, while the rest are pressure-bound with α=10-20. This result is consistent with the low star formation rate of most CMZ clouds, on the premise that stars and clusters are much less likely to form in gravitationally unbound clumps than in bound clumps.

3. Clump evolution

The large number of clumps in the CMZ sample, together with the identification of their bound and unbound populations in Section 2 above, gives an opportunity to go beyond equilibrium properties, to examine the relative time scales of clump formation and dispersal.

For this purpose the CMD in **Figure 5** was compiled for all of the CMZ clouds except Sgr B2, i.e. all CMZ clouds having a low bound clump fraction, f_b=0.06. Its shape is nearly indistinguishable from that of a log-normal distribution. For masses above the 95% completeness limit of 60 $M_\odot$, this CMD has a trend $N_C \propto M^\Gamma$ with linear power-law slope Γ=-1.2±0.1.

In a model of stopped accretion (SA), the power-law slope Γ is interpreted in terms of the relative time scales for clump accretion τ_{grow} and for accretion stopping τ_{stop}, where Γ=-τ_{grow}/τ_{stop} (Basu & Jones 2004, Basu et al. 2015, hereafter BGA15). This model allows for clumps to grow and to stop growing from a distribution of initial clump masses. The ini-
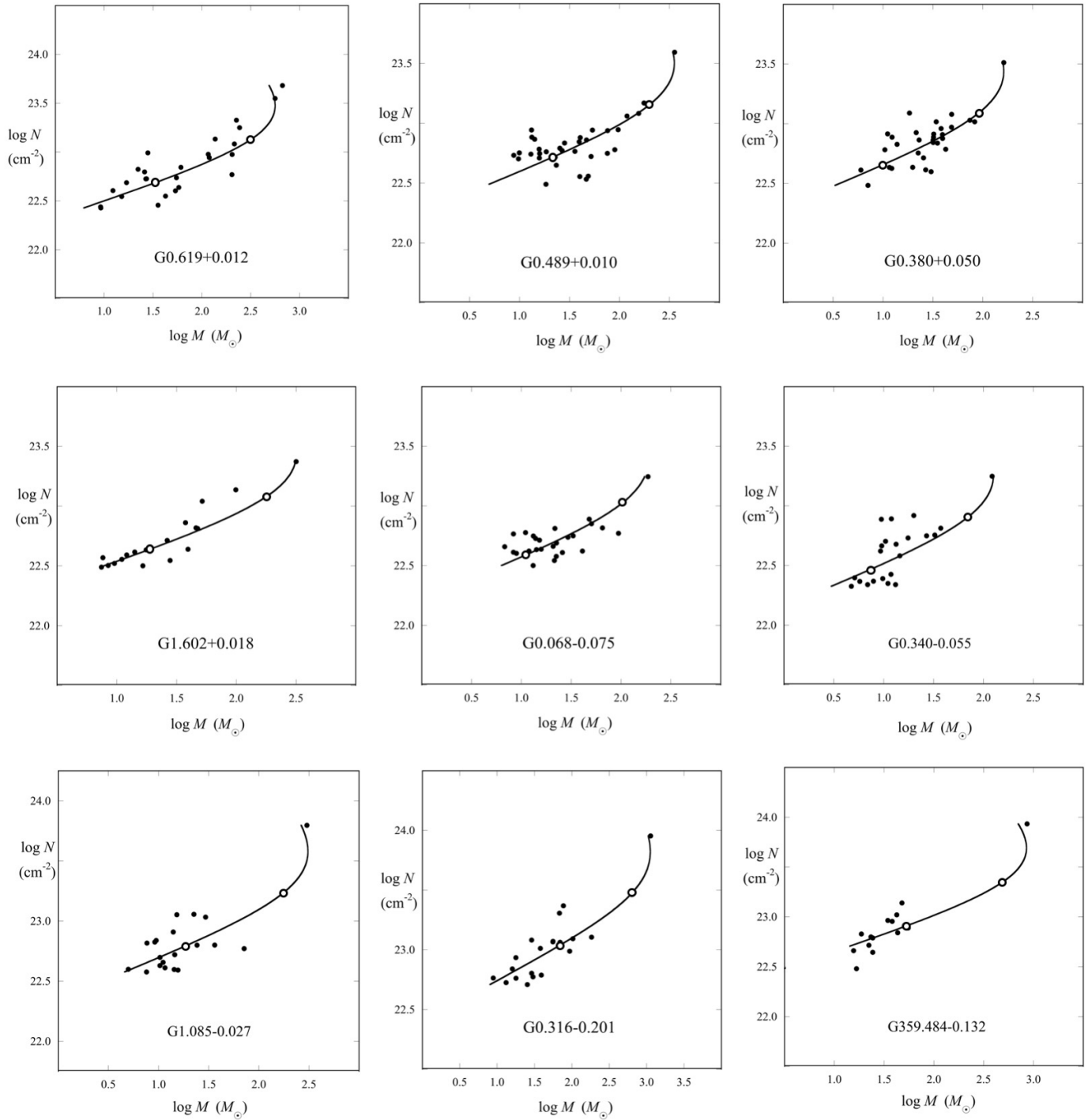
Figure 4: log *N* vs. log *M* for nine CMZ clouds whose clump population is consistent with one or two gravitationally bound clumps (upper right) and ~20 associated gravitationally unbound, pressure-bound clumps (lower left). The solid line is the best-fit PVE model. Open circles indicate virial parameter α=2, indicating the gravitationally "bound" point in Figure 1 for negligible magnetic field (upper right) and α=10 indicating points on the pressure-bound branch (lower left).
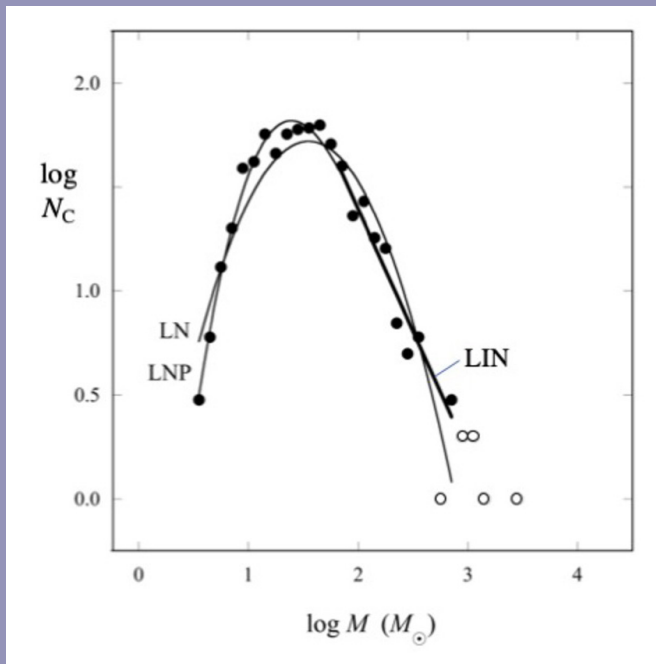
Figure 5: Clump mass distributions for CMZ populations with estimated bound clump fraction f_b=0.06. *Filled circles* indicate the log of the number of clumps N_C in a mass bin. The bin width is $\Delta \log(M/M_\odot)$=0.10, for all bins occupied by at least three clumps. *Open circles* indicate bins occupied by one or two clumps. *Light curves* are fits of log-normal (LN) and LNP models (Basu & Jones 2004) to the filled circles. *Heavy line* is a linear fit for clumps more massive than 60 $M_\odot$, the 95% completeness mass. This figure shows 670 clumps in 21 CMZ clouds, excluding Sgr B2.

tial distribution is usually assumed to be a lognormal based on the statistical central limit theorem (BGA15).

When $\Gamma\approx$-1 and the distribution evolves for many dynamical times, it develops a high-mass power-law tail, due to the small but increasing number of masses which have not stopped accreting (BGA15 Figure 1). When the distribution has evolved for less than a few dynamical times, its power-law tail is evident only as a slight asymmetry.

In Figure 5, the similarity of the CMD to a lognormal shape suggests that the mass of a typical clump in the CMZ sample may be relatively close to its formation mass. The high-mass slope $\Gamma\approx$-1 indicates that τ_{grow} and τ_{stop} are each close to the free-fall time, $\tau_f \approx$0.1 Myr based on the fits in Section 2. Together, these points suggest that the typical clump in the CMZ sample accretes mass for at most a dynamical time. However, this conclusion is limited by uncertainty in the initial clump mass distribution.

4. Summary

Star formation in the CMZ may be suppressed by a significant deficit of gravitationally bound clumps, according to virial and dynamical analyses of SMA MASSES observations, the most extensive census available of CMZ clumps. Most CMZ clouds have a bound clump fraction of ~0.06, typical clump virial parameter ~10, and similar time scales of accretion and accretion stopping, ~0.1 Myr. Gravitational binding of CMZ clumps may be weak because their turbulent motions are relatively high, as is common in the nuclear regions of barred spiral galaxies.

REFERENCES

- Basu, S., & Jones, C. 2004, MNRAS, 347, L47
- Basu, S., Gil, M., & Auddy, S. 2015, MNRAS, 449, 24 (BGA15)
- Battersby, C., Keto, E., Walker, D., et al. 2020, ApJS, 249, 35
- Bryant, A., & Krabbe, A. 2021, NewAR, 93, 101630
- Callanan, D. 2021, PhD Thesis, Liverpool John Moores University
- Federrath, C., Rathborne, J. M., Longmore, S. N., et al. 2016, ApJ, 832, 143
- Field, G., Blackman, E., & Keto, E. 2011, MNRAS, 416, 710
- Hatchfield, H., Battersby, C., Keto, E., et al. 2020, ApJS, 251, 14 (H20) Kruijssen, J., & Longmore, S. 2013, MNRAS, 435, 2598
- Kruijssen, J. M. D., Dale, J. E., Longmore, S. N., et al. 2019, MNRAS, 484, 5734
- Krumholz, M., Kruijssen, J., & Crocker, R. 2017, MNRAS, 466, 12

- Lada, C. J., Forbrich, J., Lombardi, M., & Alves, J. F. 2012, ApJ, 745, 190
- Longmore, S. N., Kruijssen, J. M. D., Bally, J., et al. 2013, MNRAS, 433, L15
- Mills, E. A. C., Corby, J., Clements, A. R., et al. 2018, ApJ, 869, 121
- Myers, P., Hatchfield, H P., & Battersby, C. 2022, ApJ, 929, 34 (MHB22)
- Rathborne, J. M., Longmore, S. N., Jackson, J. M., et al. 2014, ApJL, 795, L25
- Spitzer, L. 1978, Physical Processes in the Interstellar Medium (New York: Wiley), 241

ALMA STUDY GRANT FOR WIDEBAND CRYOGENIC ISOLATOR DEVELOPMENT

## Lingzhen Zeng, Ray Blundell, Garrett Keating, Edward Tong, Qizhou Zhang

As part of the ALMA Development Roadmap, the ALMA Board have laid out a series of fundamental scientific drivers for the next decade of development, including studying the origins and evolution of galaxies; studying the growth of chemical complexity in protostellar and protoplanetary environments; and enabling the capability for astronomers to conduct detailed imaging studies of protoplanetary disks. Enabling these scientific efforts requires significant technical development across myriad systems, but common to all is a need for additional spectral bandwidth. This increase in bandwidth will be transformative for ALMA, but requires a corresponding upgrade to the receivers. The Band6v2 project is the first effort to revamp an ALMA receiver band to increase the instantaneous bandwidth, from 5-10 GHz to eventually 4-20 GHz (Nvarrini et al. 2021).

In the SMA Receiver Lab, we have been pioneering wide IF bandwidths for more than a decade. We have demonstrated IF bandwidths in excess of 16 GHz (Zeng et al. 2018). This has been made possible by the development of a wideband 4-22 GHz cryogenic edge-mode isolator. This isolator design employs the edge mode of electromagnetic propagation in a stripline circuit on a ferrite substrate in a permanent magnetic bias field. A wideband isolator ensures a good match between the SIS mixer and the cryogenic low noise amplifier over wide bandwidths. Although a number of ALMA bands employ commercially available isolators, these do not come close to the performance required by the Band6v2 project. The isolator developed by SAO has undergone rigorous testing at the Central Development Lab of NRAO, which resulted in the SAO-developed isolator being identified as a key component of the ALMA Band6v2 development.

Recently, the SMA receiver lab was awarded a one-year ALMA study grant for wideband cryogenic isolator development focusing on three main goals:

1. **Adjust the operating band of the isolators.** To optimize the band of operation and meet the requirements of the Band6v2 project, we want to shift
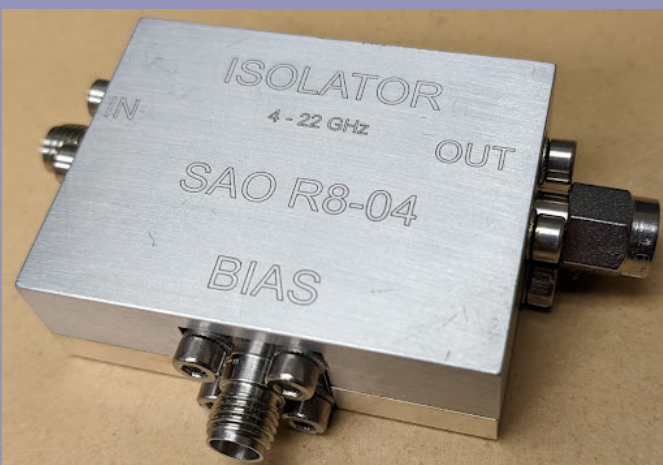
Figure 1: The R8 isolator is the latest version of the wideband cryogenic isolator developed at the SAO.

the bandwidth towards lower frequency by a linear factor of about 10%, from 4 − 22 GHz to 3.5 − 20 GHz, using a ferrite material with slightly different saturation magnetization value.

2. **Improve the performance of the isolators.** As frequency increases, more and more energy will propagate in higher order modes rather than in the fundamental edge-mode. That will cause higher insertion loss and reduced isolation. We will try different combinations of ferrite thickness and isolator circuitry to minimize the power propagating in those higher order modes.

3. **Reduce the physical dimensions and thermal mass of the isolators.** We will reduce the size of the isolator circuit and improve the mechanical design of the isolators. That will make the isolator easier to integrate into dense cryogenic systems, which is essential for future multi-detector deployments.

Each of the above goals will require multiple iterations in simulations, prototyping, and measurements. The actual isolator prototyping work requires mechanical design, machining and plating as well as processing of the ferrite, load material, circuit, and associated magnets. This development project will take place over the next 12 months, and we expect it to yield results benefiting not only ALMA, but the SMA and other radio astronomical facilities as well.

REFERENCES

- A. Navarrini, A. R. Kerr, et al 2021. ALMA Band6v2 Receiver Upgrade. doi:10.5281/zenodo.5541294

- Zeng, L., Tong, C.E., Blundell, R., et al. 2018, IEEE Transactions on Microwave Theory Techniques, 66, 2154. doi:10.1109/TMTT.2018.2799574

MEASURING THE OPTICAL PERFORMANCE OF THE WSMA RECEIVER SYSTEM

Paul Grimes, Edward Tong

Introduction

The first complete wSMA receiver prototype ("Proto-1") is currently being deployed to the SMA site on Mauna Kea, Hawaii. One of the last testing tasks that was carried out in the Receiver Lab at the CfA in Cambridge before shipping was to demonstrate the millimeter-wave optical performance of the Proto-1 system with the first two wSMA science cartridges. Achieving good optical performance that closely matches the designed characteristics is critical to achieving good coupling between the SMA antenna's beam waveguide and

Figure 1: Millimeter-wave beam scanner based on a laser engraver system installed on top of the "Proto-1" wSMA receiver system. The gold colored millimeter-wave source hardware has been mounted in place of the engraver's diode laser module.

the receiver system. This in turn is critical for achieving high aperture efficiency and low sidelobe levels from the SMA antenna system, and thus high sensitivity in SMA observations.

The wSMA receiver design incorporates features that will improve the optical performance of the receiver over that of the current SMA receiver systems. First, use of all-reflective cooled receiver optics in place of the present warm receiver selection optics and cold lenses will reduce optical loss and associated noise. Second, each wSMA cartridge receives both polarizations using a single dual-polarized feed, in contrast with the current scheme in which a large grid polarizer feeds separate singly-polarized receiver cartridges. The new scheme will assure co-alignment of both polarizations on the sky.

Optical performance measures

Signals received by an SMA antenna are directed along a beam waveguide that brings the signals to a frequency independent "virtual feed", located some distance behind the receiver. The receiver optics and feedhorn intercept this incoming beam in front of the virtual feed, and redirect and refocus the beam onto the receiver feed horns on each of the receiver cartridges. To get efficient coupling between the receiver and the telescope, we need the beam supplied by telescope's beam waveguide to match those of the beam "emitted" (we usually consider the response of the receiver to arbitrary incoming signals by imagining that the receiver is instead transmitting - i.e. as if it was operating in a time-reversed sense) from the receiver.

The most basic of the beam properties that need to be matched are the position of the beam center relative to the

nominal beam axis, and the angle of the beam propagation relative to the nominal beam axis. If both of these quantities match, then the incoming beam from the antenna is in the same location and traveling in the same direction as the beam of the receiver system. The wSMA receiver system has significant scope for aligning the plane mirror receiver optics to ensure that the receiver beam is located and pointing in the correct direction, something that can also be confirmed using optical alignment targets on the receiver cartridges with optically clear windows on the cryostat and a commercial alignment telescope.

To get efficient coupling of the receiver to the antenna, we also need to match the size of the antenna and receiver beams, and to match phase curvature of the beams. The size of a two-dimensional Gaussian beam is described by a beam width in each of the two orthogonal directions, defined as the distance from the beam center where the electric field strength falls by 1/e. The beam width and phase curvature is measured by mapping the amplitude and phase distribution of the receiver response, and fitting a Gaussian function to the response pattern.

Coherent beam scanning

Determining these beam characteristics requires that we measure both the amplitude and phase response of the receiver system. To do this, we take advantage of the fact that the wSMA receivers are coherent receivers, able to downconvert incoming millimeter-wave signals to lower frequencies, preserving both amplitude and phase. By scanning a millimeter-wave source with known amplitude and phase across a plane in front of the wSMA receiver, we can measure the spatial dependence of the amplitude and phase response of the wSMA receiver system. This coherent beam scanning technique has previously been used with the original SMA receivers[1], and is closely related to the coherent holographic techniques used to measure the optical performance of the SMA antenna surfaces[2].

The major changes to the previous beam scanning system necessary for use with the wSMA receivers are to increase the area scanned by the beam scanner, and to use RF lock-in amplifiers in place of the now obsolete vector voltmeters.

We have developed a wider area scanning system by adapting a "maker" grade laser engraving system with a 300 mm square range of motion, replacing the diode laser module with a millimeter-wave source on a 3d printed mount (Fig. 1). This system provides a cost-effective source of X-Y motion components, as well as a controller running open-source control firmware that can easily be interfaced to Python software over USB. This beam scanner unit was installed on top of the
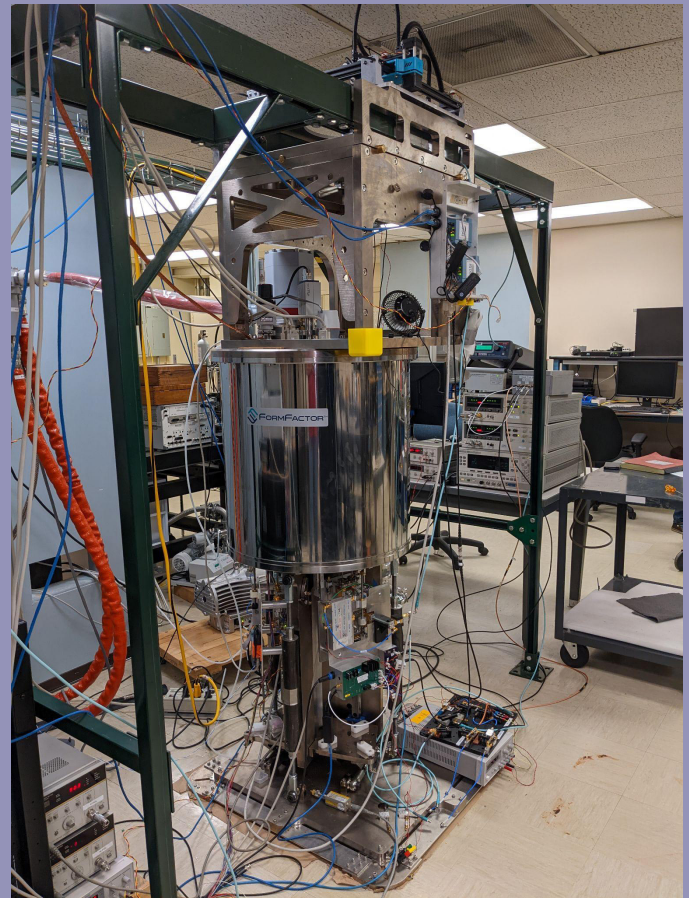

Figure 2: The "Proto-1" wSMA receiver system, set up for millimeter wave beam scanning. The beam scanner system is installed on the very top of the receiver system. On the floor beside the wSMA receiver is the "RF-plate" that down-converts the IF signals from the two active receiver channels, and the IF signal from the harmonic mixer monitoring the millimeter-wave source amplitude and phase. These signals are then amplified and compared by two RF lock-in amplifiers on the table behind the wSMA receiver system.

wSMA receiver's "optical alignment interface" in roughly the position that the SMA's M6 mirror would normally sit (Fig. 2).

The millimeter-wave source is based on a chain of multipliers and amplifiers with a total multiplication factor of 18 from the master synthesizer that generates the fundamental tone. The wSMA SIS receivers are driven by a single wSMA prototype Local Oscillator (LO) module, phase locked to a 109 MHz reference source. The ~4.8 GHz IF signal from the SIS receivers are down-converted to an IF of 86.85 MHz and filtered and amplified before being measured by the RF lock-in amplifiers. The RF lock-in amplifiers are referenced to the third harmonic of a ~28.5 MHz IF generated from the wSMA LO module. All fundamental and reference sources, as well

[1] Christensen, Robert D., et al. *"Vector Near-Field Beam Scanner for the SMA"*, SPIE, 2014, pp. 915330–915330–8, https://doi.org/10.1117/12.2057124
[2] Sridharan, Tirupati K., et al. *"Holographic Surface Setting of the Sub-Millimeter Array Antennas"*, SPIE, 2004, pp. 441–46, https://doi.org/10.1117/12.550939
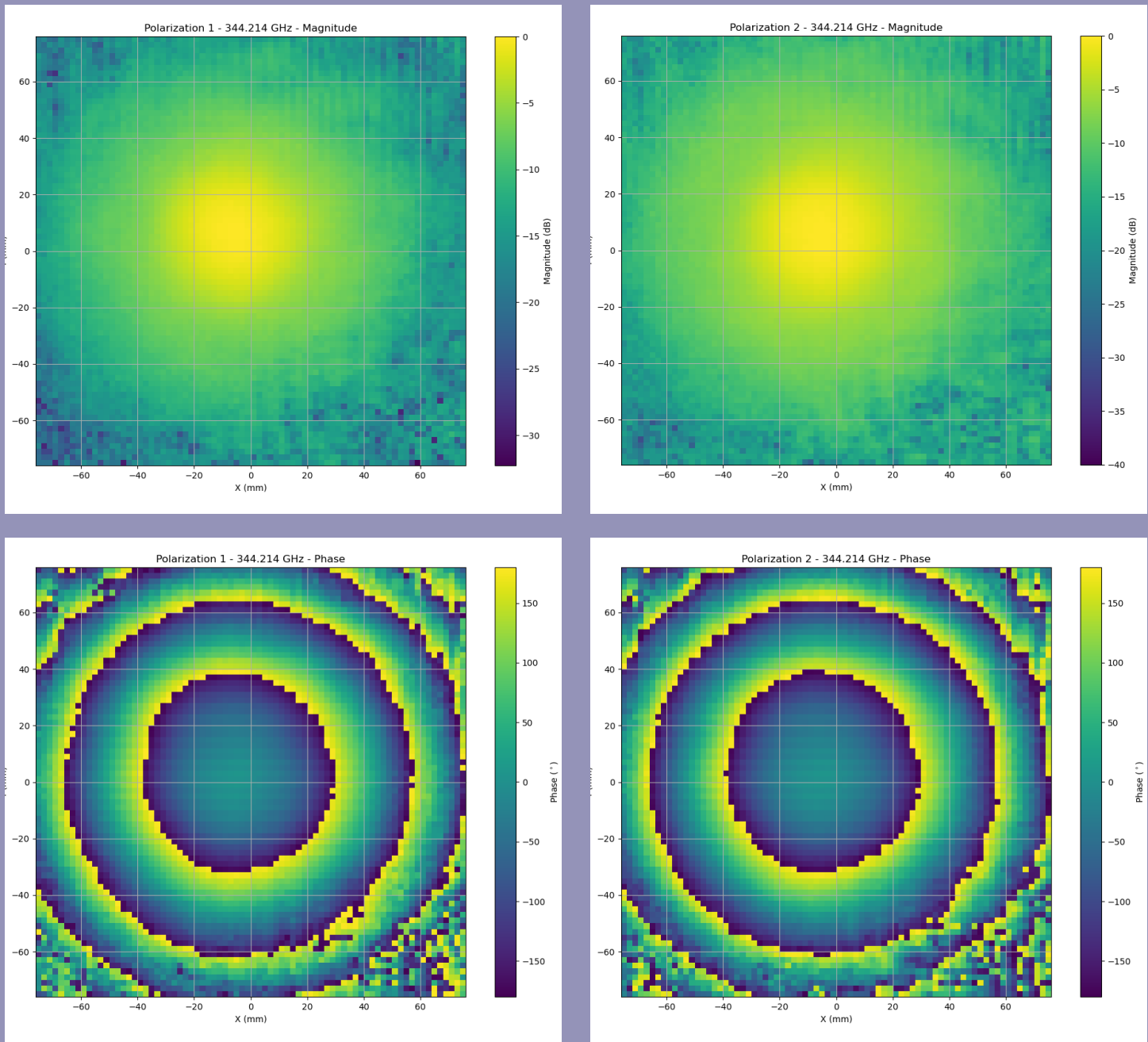
Figure 3: Measured power (magnitude) and phase maps for the two polarization channels of the Proto-1 High band receiver cartridge. These maps show some position misalignment from the center of the beam scanner (which can easily be adjusted during receiver optics alignment), and excellent co-alignment between the two polarizations.

as the RF lock-in amplifiers, are synchronized to a 10 MHz reference signal generated by a Stanford Research Systems rubidium frequency standard.

This coherent beam scanning system has demonstrated excellent performance, with > 50 dB dynamic range and short term amplitude and phase stability of ±0.1 dB and ±5°. Longer term stability is affected by temperature changes in the Receiver Lab, which we mitigate by taking frequent calibration measurements during the automated scanning routine.

One useful feature of this beam scanning system is that it measures the optical performance of two SIS receiver channels simultaneously. By setting the polarization of the millimeter wave source (by rotating it in its mount) to 0°, 90°, or 45°, we can measure the co- and cross-polarization response for the two receiver channels, or we can simultaneously measure the co-polarized response of both channels of the receiver.

Proto-1 Optical Performance

Over approximately two months at the end of 2022, we carried out several beam scanning exercises using the first two Low and High band wSMA receiver cartridges as we have developed the beam scanning system and the wSMA receivers and local oscillator units. An example beam map is shown in Fig. 3. All measurements have shown excellent alignment between the two orthogonal polarization channels within each receiver cartridge. The misalignment between orthogonal polarization channels at the same frequency has been a significant source of reduced efficiency in recent SMA polarization observations with the original SMA receivers, due to the independent receiver cartridges and optics for each polarization signal.

The absolute alignment of the receivers has generally been good, with beam position misalignments of less than 10% of a beam width for both cartridges, and excellent repeatability between receiver cooldowns. Additional alignment will be required once the receiver is operating at the SMA site, as the reduced ambient pressure at altitude will affect the receiver alignment, but we believe that we now have all the tools in place to quickly realign the system during on-site deployment.

While the position and angles of the receiver beams can be adjusted by adjusting alignment of the plane mirrors and grids in the wSMA receiver's optical system, the phase curvature and beam width of each of the receivers is not easily adjustable, but is set by the design of the feed and fixed receiver cartridge focussing mirrors. Thus the measurement of the beam width and radius of phase curvature is key to verifying the optical performance of the receiver before deployment to the SMA site.

To calculate the Gaussian beam parameters from the measured amplitude and phase maps of the receiver beams, we can use a variety of fitting techniques, from simple fitting of a two-dimensional Gaussian to the amplitude map and a quadratic surface to the phase map, to Laguerre-Gaussian mode expansion of the measured complex beam maps. These fitting algorithms are still under development for this particular system, but in Figs. 4 and 5 we show preliminary results for the beam width and radii of phase curvature for the Proto-1 receivers, established using the simplest Gaussian fitting method, along with the Gaussian beam parameters expected from the nominal design.

The results shown in Figs. 4 and 5 suggest that the beam widths and focus are close to the design values of the receiver optical system (within the uncertainties introduced by the fitting methods and measurement noise), and that we should expect efficient optical coupling from the Proto-1 wSMA receiver when deployed on an SMA antenna.

Next Steps

During the deployment of the Proto-1 wSMA receiver to the SMA site, we will be carrying further optical and millimeter-wave alignment and optical measurements in the receiver lab in the SMA hangar, which will allow us to gather measurements over a wider range of frequencies in an environment that is much closer to that of the SMA antennas.

Once the smooth operation of the Proto-1 receiver is established in the SMA hangar, it will be installed into a SMA antenna for on-sky testing. As part of these trials, we will measure the optical efficiency, beam patterns and other optical performance of the SMA antenna using the current SMA receiver, before replacing the SMA receiver with the Proto-1 wSMA receiver. This will allow us to make direct comparisons of the optical performance of the wSMA receiver with the existing SMA receivers.
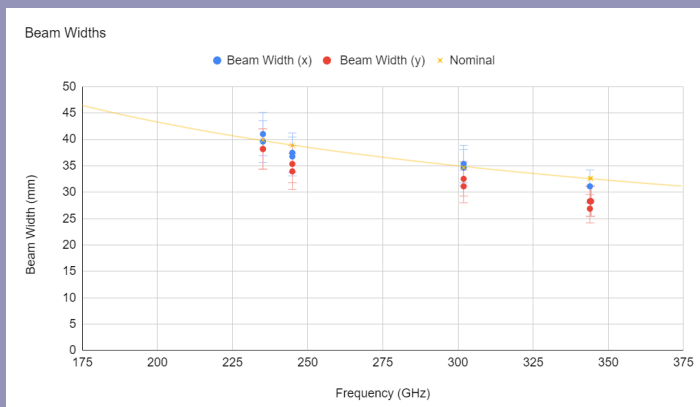

Figure 4: Beam widths measured for the Proto-1 wSMA receiver system, across both Low and High band receiver cartridges.
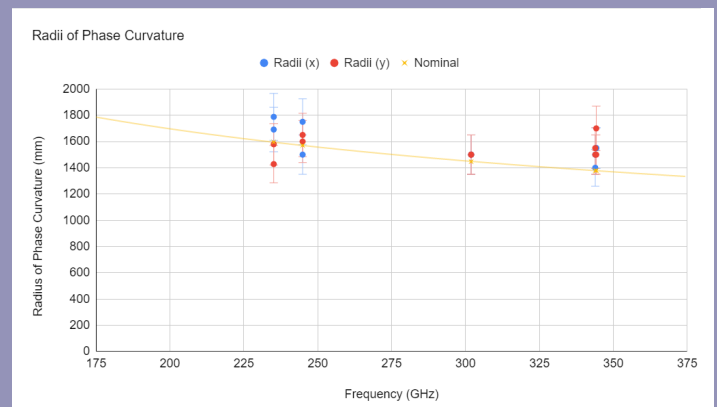

Figure 5: Radii of the phase curvature measured for the Proto-1 wSMA receiver system, across both Low and High band receiver cartridges.

SMA & THE MAUNA LOA VOLCANO ERUPTION

The Mauna Loa volcano eruption was a beautiful display of Mother Nature mixed with Hawaiian tradition, culture, and lots of history. On November 27, 2022 @ 23:30 HST, Mauna Loa, the world's largest active volcano, erupted. The eruption lasted for a total of 12 days and was producing between 50 and 100 cubic yards of lava per second. According to the United States Geological Survey (USGS), lava broke to the surface within Moku'aweoweo, the summit caldera on Mauna Loa, for the first time in 38 years. This was Mauna Loa's longest quiet period in recorded history (USGS.gov, 2022). The last eruption occurred in 1984. Pele (the goddess of fire, lighting, wind, dance and volcanoes), is the Hawaiian volcano deity, an elemental force, and the creator of volcanic landscapes. What was Pele going to do, and what did we need to prepare for? Possible road closures due to lava flow, volcanic smog (VOG), Pele's hair (volcanic glass), and traffic congestion due to sightseers were a few of the issues SMA had to manage safely.

On November 28, and the days to follow, Pele determined that the Mauna Loa lava flow would make its way down slope toward the north/northeast side of the island with the direct path headed for Daniel K. Inoye State Highway (Saddle Road). Saddle Road is the main link between the East and West side of the island. If overtaken by lava, the damage would have a detrimental effect on everyone island wide, including SMA operations. Contingency plans had to be made, including alternative routes to the Maunakea summit (dormant volcano where the SMA facility is located) and adjusted work schedules. A typical trip to the summit takes about two hours. This includes a 30 minute acclimation period half way up the mountain. If Saddle Road is closed and our main access is blocked, we would have to take the "back" Mauna Road. Mauna Road requires 4WD, that would easily take over 4 hours, not including acclimation, to get up to the summit. Additionally, only experienced drivers would be allowed to make that journey. Although the route up north to Mauna Road is a beautiful ocean scenic drive, traffic would become an issue. This new route would become the new Saddle Road until repairs could be made. Traffic, long commutes, and lava flow weren't the only things the SMA had to worry about, VOG, Pele's Hair, and traffic congestion also posed additional hazards and challenges.
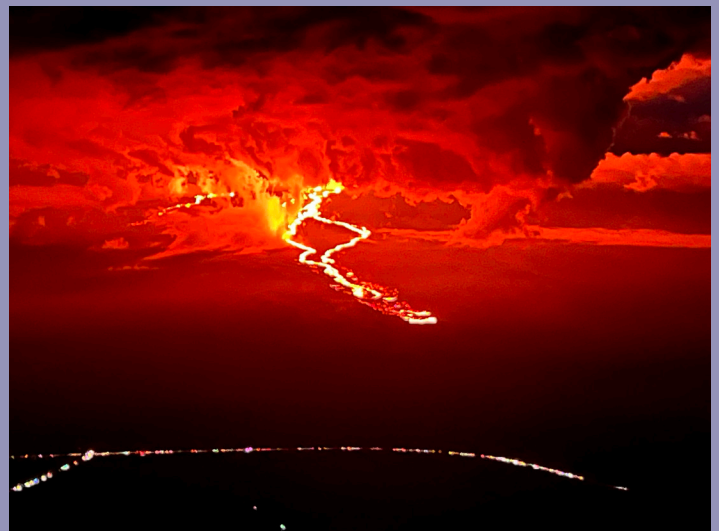
Figure 1: Photographs of Mauna Loa volcano eruption during 2022 (taken by Clint Monceaux). The lava flows are visible. The long stretch of lights near the bottom of the photographs were from vehicles of sightseers.

VOG and Pele's Hair were two additional hazards associated with the eruption. VOG, according to the International Volcanic Health Hazard Network (IVHHN), is a hazy mixture of SO_2 gas and aerosols (tiny particles or droplets) which are primarily sulfuric acid and other sulfate compounds (vog.ivhhn.org, 2022). Depending on Pele's wind direction, SMA summit staff could find themselves downwind and exposed. Fortunately, with the exception of one day, wind direction was in our favor and the SMA was able to continue daily operations. We did, however, need to prepare for what we found next.

It just so happened snow fell on Maunakea at the same time the eruption was occurring. It's pretty fascinating to be standing on one snow-covered volcano looking across the island at another spewing lava. This was a definite first for SMA staff. When walking around the snow covered ground, one of the SMA staff pointed to a tiny strand that looked like a human hair or a part of a spider's web. Hobart King, writer for geology.com and author of "Pele's Hair and Pele's Tears: Among the most unusual types of lava", writes that Pele's hair is the name given to hair-like strands of volcanic glass that are stretched from still-molten masses of lava as they are launched or fall through the air at a lava fountain, a lava cascade, or a spatter cone (King, 2022). These strands of hair like glass fibers can get up to two feet in length but only one micron (.001 mm) thick. As spectacular as they are, Pele's Hair must be treated with caution, as its tiny sharp strands of glass can penetrate skin and enter the eyes. We were lucky enough to not have any issues with Pele's Hair and continued to keep a close eye on things in case it got worse.

With the announcement of the eruption, sightseers soon followed. On one particular afternoon, some of us were working late completing the annual fire alarm testing at the summit. When we made our decent, we were fortunate enough to have the most amazing view of the lava fountain, lava flow, and night sky (see Figure 1). Naturally we stopped to take many pictures and quietly soak in this once in a lifetime natural wonder. After taking pictures, we looked down and wondered what all those tiny lights were on Saddle Road. The lights were endless and stretched for miles. We realized the lights were cars of sightseers. It seemed like the entire island was coming to see the eruption. As we approached Saddle Road, what was a 60mph highway was now a 5mph traffic jam. People were everywhere. The county and state eventually issued a notification stating that there would be a $1000.00 fine for anyone parking, walking, or standing on the main highway. Thankfully, no major incidents were reported and all SMA staff got to work and home safely.

On December 13, 2022, the Hawaiian Volcano Observatory announced that Mauna Loa was no longer erupting. Lava rested 1.8 miles away from Saddle Road, and VOG was no longer an issue. Being close to the world's largest active volcano, we all were a bit on edge and didn't know what to expect. Hawaii's Kilauea (Mauna Loa's neighboring volcano) 2018 eruption caused a considerable amount of damage that destroyed over 700 homes and displaced thousands of residents. We are thankful that Mauna Loa is resting for now. Still active, it is currently showing no signs of major activity. This eruption was indeed a very unique experience that the professional and dedicated SAO/SMA staff will forever remember. Hawaii is a beautiful place to live and work. Hopefully, this experience will be a once in a lifetime event!

Story and photos by Clint Monceaux, Safety Coordinator of the SMA

REFERENCES:

- King, H. (n.d.). Pele's hair and Pele's tears. geology. Retrieved December 29, 2022, from https://geology.com/volcanoes/peles-hair/
- International Volcanic Health Hazard Network . (2022, December). What is Vog? IVHHN. Retrieved December 29, 2022, from https://vog.ivhhn.org/what-vog
- USGS. (2022, December 10). November 27-December 10, 2022. Mauna Loa had not erupted since 1984—its longest quiet period in recorded history. Retrieved December 29, 2022, from https://www.usgs.gov/volcanoes/mauna-loa/november-27-december-10-2022

Photo credit: Shelbi Schimpf, CMZoom Team

www.cfa.harvard.edu/sma-school   sma-school@cfa.harvard.edu

2023 SUBMILLIMETER ARRAY INTERFEROMETRY SCHOOL

The Center for Astrophysics, in conjunction with the Academia Sinica Institute of Astronomy and Astrophysics and the University of Hawaii, invite you to apply to the 2023 Submillimeter Array Interferometry School. The school will be held at the Center for Astrophysics in Cambridge, MA, from 15-19 May 2023, with limited space for virtual participation.

The main goals of the school are to provide graduate students, postdocs and scientists outside the field with a broad knowledge of interferometry and data reduction techniques, with a special emphasis on the Submillimeter Array (SMA) interferometer and its new capabilities. The school will also extensively utilize the SMA, located on Maunakea, providing a hands-on experience of performing observations and data reduction for projects proposed by school participants. Successful applicants will be awarded observing time on the SMA, data from which will be used as part of the activities of the school.

Applications for the school are open until January 30, 2023. Further details can be found on the school website.

Website: **https://www.cfa.harvard.edu/sma-school/program**

Contact: **sma-school@cfa.harvard.edu**

SMA POSTDOCTORAL FELLOWS: COMINGS AND GOINGS

The Submillimeter Array Postdoctoral Fellowship program supports early career scientists active in a variety of astronomical research fields involving submillimeter astronomy. The SMA Fellowship is competitive, and a high percentage of our past Fellows have gone on to permanent faculty and research staff positions located around the world.

The SMA welcomes our newest Fellows:

Joshua Lovell completed his Ph.D. work at Cambridge University in 2022, with the thesis 'High resolution studies of planetary systems' (advisor: Mark Wyatt). Joshua's research is focused on gas and dust in protoplanetary disks around pre-main sequence stars, and their evolution.

Jakob den Brok completed his Ph.D. work at University of Bonn, Germany in 2022, with the thesis 'Molecular Gas Physics and Chemistry Across Nearby Galaxies' (adviser: Frank Bigiel). Jakob's research is in observational astronomy related to interstellar medium in galaxies, with particular interests in studying the molecular gas in nearby galaxies.

Lovell and den Brok started their fellowship in fall 2022. They join continuing SMA Fellows Eric Koch and Kirsten Hall.

We wish all our current and former Fellowship holders continued success!

A list of current and former SMA Fellows is provided at:

https://pweb.cfa.harvard.edu/opportunities/fellowships-visiting-scientist-positions/sma-postdoctoral-fellowships

along with further information on the SMA Fellowship program and future SMA Fellowship opportunities.

Qizhou Zhang
Chair, SMA Fellowship Selection Committee

CALL FOR STANDARD OBSERVING PROPOSALS - 2023A SEMESTER

We wish to draw your attention to the next Call for Standard Observing Proposals for observations with the Submillimeter Array (SMA). This call is for the 2023A semester with observing period **23 May 2023 – 15 Nov 2023.**

Standard Observing Proposals Submission deadline: **Thursday, 2 March 2023 21:00 UTC (4PM EST)**

The full Call for Proposals, with details on time available and the proposal process, will be available by February 2 at the SMA Observer Center (SMAOC) at **http://sma1.sma.hawaii.edu/call.html.**

Details on the SMA capabilities and status can be found at **http://sma1.sma.hawaii.edu/status.html;** proposal creation and submission is also done through the SMAOC at **http://sma1.sma.hawaii.edu/proposing.html.** We are happy to answer any questions and provide assistance in proposal submission; simply email **sma-propose@cfa.harvard.edu** with any inquiries.

Sincerely,

Mark Gurwell, SAO Chair, SMA TAC

Ya-Wen Tang, ASIAA Chair, SMA TAC

PROPOSAL STATISTICS FOR 2022B

The three SMA partner institutions received a total of 45 proposals (SAO 38, ASIAA 6, UHawaii 1) requesting observing time in the 2022B semester. In the Call for Proposals for 2022B, SAO proposers were notified that there was a delayed start to the semester (to December 8, 2022), and that there would be a science hiatus for part of February. Since the call, SAO has approved 2 DDT proposals and ASIAA has approved 1 DDT proposal. The 48 proposals were divided among science categories as follows:

CATEGORY	PROPOSALS
local galaxies, starbursts, AGN	12
protoplanetary, transition, debris disks	8
submm/hi-z galaxies	8
high mass (OB) star formation, cores	6
low/intermediate mass star formation, cores	4
GRB, SN, high energy	4
evolved stars, AGB, PPN	2
solar system	2
galactic center	1
other	1

TRACK ALLOCATIONS BY WEATHER REQUIREMENT AND CONFIGURATION:

To best accomodate the highest ranked programs from each of the partners, it was determined that the configuration schedule would be: VEX >> SUB >> COM >> EXT >> VEX

PWV[1]	SAO	ASIAA	UH[2]
< 4.0mm	20A + 41B	7A + 6B	0
< 2.5mm	17A + 14B	2A + 4B	4
< 1.0mm	3B	0	0
Total	**37A + 58B**	**9A + 10B**	**4**

Configuration	SAO	ASIAA	UH[2]
Subcompact	10A + 12B	1A + 5B	0
Compact	12A + 19B	3A + 3B	0
Extended	7A + 7B	1A	0
Very Extended	6A + 3B	3A + 1B	0
Any	2A + 17B	1A + 1B	4
Total	**37A + 58B**	**9A + 10B**	**4**

(1) Precipitable water vapor required   (2) UH does not list As and Bs.
   for the observations.

TOP-RANKED 2022B SEMESTER PROPOSALS

The following is the listing of all SAO, ASIAA, and UH proposals with at least one A-rank track allocation.

EVOLVED STARS, AGB, PPN
2022B-S019   Joel Kastner (RIT): *Mapping the Complex Molecular Envelope of the Planetary Nebula NGC 3132*

GALACTIC CENTER
2022B-S025   Garrett "Karto" Keating (CfA): *Polarimetric VLBI for the 2023 Event Horizon Telescope Campaign*

GRB, SN, HIGH ENERGY
2022B-A002   Kuiyun Huang (CYCU): *Electro-magnetic wave candidate of IceCube Neutrino event*
2022B-S009   Tianyu Tu (Nanjing): *Shock and cosmic ray chemistry in molecular clouds interacting with supernova remnant W28*
2022B-S013   Anna Ho (Cornell): *The Landscape of Relativistic Stellar Explosions*

HIGH MASS (OB) STAR FORMATION, CORES
2022B-A003   Natsuko Izumi (ASIAA): *Core Mass Function in Metal-Poor Environment*
2022B-A004   Greta Hiu Lam Siu (NTHU): *Turbulence and magnetic fields in high mass star forming clumps*
2022B-S007   Qizhou Zhang (CfA): *What drives the starburst in W49A?*

LOCAL GALAXIES, STARBURSTS, AGN
2022B-S021   Jean Turner (UCLA): *CO(3-2) in the Dwarf Galaxy NGC 1569*
2022B-S034   Jakob den Brok (CfA): *A wide-band high-resolution molecular survey in the starburst M82*
2022B-S040   Fabio Pacucci (CfA): *Unveiling the Spectral Energy Distribution of the SMBH at the Center of Leo I*

PROTOPLANETARY, TRANSITION, DEBRIS DISKS
2022B-H001   Jonathan Williams (UH): *The chemical composition of gas in the disk-clearing phase of planet formation*
2022B-S002   David Wilner (CfA): *An Imaging Survey of Forgotten Nearby Herbig Ae/Be Stars (redux, part 2)*
2022B-S015   Sean Andrews (CfA): *Detailed (Sub)Millimeter Continuum Spectra of Protoplanetary Dust Disks*

SOLAR SYSTEM
2022B-S012   Nathan Roth (NASA GSFC): *Coordinated SMA/JWST Studies of Comet C/2022 E3: Inner Coma Thermal Physics and a Window into Sulfur Chemistry*

SUBMM/HI-Z GALAXIES
2022B-S039   Luwenjia Zhou (Nanjing): *A systematic survey on the dust/gas emission of cluster galaxies in the early Universe*

STANDARD, DDT, AND LARGE SCALE PROJECTS OBSERVED DURING 2022A

SMA Semester 2022A encompassed the period June 15, 2022 through December 7, 2022, with some overlapping projects requiring VEX configuration observed into early January 2023. Listed below are all SMA standard and DDT projects that were at least partially completed during the SMA Semester 2022A.

EVOLVED STARS, AGB, PPN
2022A-S030   Megan Lewis (N.Copernicus): *SiO maser signatures of nearby evolved stars*
2022A-S032   Sofia Wallström (KU Leuven): *The Nearby Evolved Stars Survey: Exploring the inner AGB wind*

GRB, SN, HIGH ENERGY
2022A-S019   Anna Ho (Cornell): *The Landscape of Relativistic Stellar Explosions*
2022A-S039   Kishalay De (MIT): *Search for molecular emission in an exceptional Galactic stellar merger candidate*
2022A-S053*   Lauren Rhodes (Oxford): *DDT: GRB 221009A*
2022A-S054*   Yvette Cendes (CfA): *DDT: Observations of GRB 221009A*
2022A-A015*   Kuiyun Huang (CYCU): *DDT: Swift J1913.1+1946*

HIGH MASS (OB) STAR FORMATION, CORES
2022A-A003   Seamus Clarke (ASIAA): *Linking the fragmentation of clumps to the relative importance of gravity, turbulence and magnetic fields on multiple scales*
2022A-A007   Han-Tsung Lee (ASIAA/NCU): *Probe the multiscale magnetic field toward the filamentary infrared dark cloud SDC18*
2022A-A012   Hau-Yu Baobab Liu (ASIAA): *Turbulence and magnetic fields in high mass star forming clump G31 and DR21*
2022A-H004   Adwin Boogert (IfA/UH): *Resolving disks in the massive protostellar binary W3 IRS5*
2022A-S006   Jonathan Tan (UVirgina): *A Spectral Line Survey of Clustered Massive Protostars to Probe the Astrochemical Evolutionary Sequence*
2022A-S013   Pamela Freeman (UCalgary): *Where are the Carbon Chain Molecules in DR21(OH)?*
2022A-S017   Manuel Fernandez Lopez (IAR): *Dispersal explosive outflows in massive star-forming regions: more common than thought? Confirming the trend in S106IR.*
2022A-S018   Qizhou Zhang (CfA): *What drives the mini starburst in Sgr B2?*
2022A-S026   Todd Hunter (NRAO): *Triggered follow-up of accretion outbursts in massive protostars*
2022A-S033   Daria Dall'Olio (Chalmers): *Unveling magnetic fields in the high-mass star-forming region G24.78+0.08*
2022A-S036   Fengwei Xu (Peking U.): *Investigate the Fragmentation by SMA Inside the Gas Infalling Massive Clumps*
2022A-S040   Junhao Liu (EAO): *A pilot dust polarization survey of massive dense cores in Cygnus-X*

LOCAL GALAXIES, STARBURSTS, AGN
2017B-S075   Jan Forbrich (UHertfordshire): *SMA Survey of Resolved Dust and Simultaneous CO Observations of GMCs in M31 [Large Scale Program]*
2022A-S004   Gerrit Schellenberger (CfA): *Probing the high frequency variability of NGC5044: the key to AGN feedback*
2022A-S010   Giovanni Fazio (CfA): *Observations of the cold molecular gas in the barred spiral galaxy HE0045-2145*
2022A-S022   Eric Koch (CfA): *A resolved molecular gas survey of the edge-on galaxy NGC 891*
2022A-S023   Eric Koch (CfA): *Resolving the molecular gas fuelling IC 10's starburst on 2.5 pc scales*
2022A-S029   Cosima Eibensteiner (UBonn): *Untangling the molecular gas physics in the center of the starburst galaxy NGC 6946*
2022A-S034   Glen Petitpas (MIT): *The Beautiful and Enigmatic Spiral Galaxy NGC 7331*
2022A-S043   Steven Willner (CfA): *Disentangling radiating particle properties and jet physics from M87 multi-wavelength variability*
2022A-S047   Ioannis Myserlis (IRAM): *SMAPOL: SMA Monitoring of AGNs with POLarization*
2022A-S052   Eric Koch (CfA): DDT: *Combining the SMA and JWST to confirm a young massive cluster progenitor in M33*

*All three of the DDT requests were received within a short time window and accepted; data was obtained under 2022A-S053

LOW/INTERMEDIATE MASS STAR FORMATION, CORES

2022A-A013   Hau-Yu Baobab Liu (ASIAA): *Does Converging Flows or Magnetic Fields Drive the Differential Evolution of L1287?*

2022A-S007   Carlos Eduardo Muñoz-Romero (CfA): *Resolving the Chemical Evolution of Class 0/I Protostars in Perseus*

2022A-S008   Jennifer Bergner (UChicago): *Molecular mapping of the chemically rich outflow B1-a*

OTHER

2022A-H003   Jason Hinkle (IfA/UH): *Rainbow tide: multi-wavelength follow-up of tidal disruption events*

2022A-S055   Michael McCollough (CfA): *A Request for Simultaneous SMA and IXPE Polarization Observations (of Cyg X-3)*

PROTOPLANETARY, TRANSITION, DEBRIS DISKS

2022A-S011   Feng Long (UArizona): *Mapping the Gas Environment of Heavily Veiled Young Stars*

SOLAR SYSTEM

2022A-A006   Wei-Ling Tseng (NTNU): *Monitoring Io's dynamical volcanic eruptions and their contributions to Jupiter's magnetosphere*

SUBMM/HI-Z GALAXIES

2022A-H002   Lennox Cowie (IfA/UH): *Developing a sample of faint submm sources and determining their properties*

2022A-S014   Giovanni Fazio (CfA): *Understanding the Evolution of Obscured Activity Out to z>3 — An Initial Phase SMA Survey of Submillimeter Sources in the JWST Time Domain Field*

2022A-S041   Xiurui Zhao (CfA): *Mornitoring with SMA a Highly Variable Flat Spectrum Radio Quasar in the JWST North Ecliptic Pole Time-Domain Field*

RECENT PUBLICATIONS

TITLE: A very luminous jet from the disruption of a star by a massive black hole

AUTHOR: Andreoni, I., Coughlin, M. W., Perley, D. A., Yao, Y., Lu, W., Cenko, S. B., Kumar, H., Anand, S., Ho, A. Y. Q., Kasliwal, M. M., de Ugarte Postigo, A., Sagués-Carracedo, A., Schulze, S., Kann, D. A., Kulkarni, S. R., Sollerman, J., Tanvir, N., Rest, A., Izzo, L., Somalwar, J. J., Kaplan, D. L., Ahumada, T., Anupama, G. C., Auchettl, K., Barway, S., Bellm, E. C., Bhalerao, V., Bloom, J. S., Bremer, M., Bulla, M., Burns, E., Campana, S., Chandra, P., Charalampopoulos, P., Cooke, J., D'Elia, V., Das, K. K., Dobie, D., Agüí Fernández, J. F., Freeburn, J., Fremling, C., Gezari, S., Goode, S., Graham, M. J., Hammerstein, E., Karambelkar, V. R., Kilpatrick, C. D., Kool, E. C., Krips, M., Laher, R. R., Leloudas, G., Levan, A., Lundquist, M. J., Mahabal, A. A., Medford, M. S., Miller, M. C., Möller, A., Mooley, K. P., Nayana, A. J., Nir, G., Pang, P. T. H., Paraskeva, E., Perley, R. A., Petitpas, G., Pursiainen, M., Ravi, V., Ridden-Harper, R., Riddle, R., Rigault, M., Rodriguez, A. C., Rusholme, B., Sharma, Y., Smith, I. A., Stein, R. D., Thöne, C., Tohuvavohu, A., Valdes, F., van Roestel, J., Vergani, S. D., Wang, Q., Zhang, J.

PUBLICATION: *Nature, 612, 430-434*

PUBLICATION DATE: Dec-22

ABSTRACT: https://ui.adsabs.harvard.edu/abs/2022Natur.612..430A

DOI: 10.1038/s41586-022-05465-8

TITLE: X-ray Polarization Observations of BL Lacertae

AUTHOR: Middei, R., Liodakis, I., Perri, M., Puccetti, S., Cavazzuti, E., Di Gesu, L., Ehlert, S. R., Madejski, G., Marscher, A. P., Marshall, H. L., Muleri, F., Negro, M., Jorstad, S. G., Agís-González, B., Agudo, I., Bonnoli, G., Bernardos, M. I., Casanova, V., García-Comas, M., Husillos, C., Marchini, A., Sota, A., Kouch, P. M., Borman, G. A., Kopatskaya, E. N., Larionova, E. G., Morozova, D. A., Savchenko, S. S., Vasilyev, A. A., Zhovtan, A. V., Casadio, C., Escudero, J., Myserlis, I., Hales, A., Kameno, S., Kneissl, R., Messias, H., Nagai, H., Blinov, D., Bourbah, I. G., Kiehlmann, S., Kontopodis, E., Mandarakas, N., Romanopoulos, S., Skalidis, R., Vervelaki, A., Masiero, J. R., Mawet, D., Millar-Blanchaer, M. A., Panopoulou, G. V., Tinyanont, S., Berdyugin, A. V., Kagitani, M., Kravtsov, V., Sakanoi, T., Imazawa, R., Sasada, M., Fukazawa, Y., Kawabata, K. S., Uemura, M., Mizuno, T., Nakaoka, T., Akitaya, H., Gurwell, M., Rao, R., Di Lalla, N., Cibrario, N., Donnarumma, I., Kim, D. E., Omodei, N., Pacciani, L., Poutanen, J., Tavecchio, F., Antonelli, L. A., Bachetti, M., Baldini, L., Baumgartner, W. H., Bellazzini, R., Bianchi, S., Bongiorno, S. D., Bonino, R., Brez, A., Bucciantini, N., Capitanio, F., Castellano, S., Ciprini, S., Costa, E., De Rosa, A., Del Monte, E., Di Marco, A., Doroshenko, V., Dovčiak, M., Enoto, T., Evangelista, Y., Fabiani, S., Ferrazzoli, R., Garcia, J. A., Gunji, S., Hayashida, K., Heyl, J., Iwakiri, W., Karas, V., Kitaguchi, T., Kolodziejczak, J. J., Krawczynski, H., La Monaca, F., Latronico, L., Maldera, S., Manfreda, A., Marin, F., Marinucci, A., Massaro, F., Matt, G., Mitsuishi, I., Ng, C.-Y., O'Dell, S. L., Oppedisano, C., Papitto, A., Pavlov, G. G., Peirson, A. L., Pesce-Rollins, M., Petrucci, P.-O., Pilia, M., Possenti, A., Ramsey, B. D., Rankin, J., Ratheesh, A., Romani, R. W., Sgró, C., Slane, P., Soffitta, P., Spandre, G., Tamagawa, T., Taverna, R., Tawara, Y., Tennant, A. F., Thomas, N. E., Tombesi, F., Trois, A., Tsygankov, S., Turolla, R., Vink, J., Weisskopf, M. C., Wu, K., Xie, F., Zane, S.

PUBLICATION: *arXiv e-prints, arXiv:2211.13764*

PUBLICATION DATE: Nov-22

ABSTRACT: https://ui.adsabs.harvard.edu/abs/2022arXiv221113764M

TITLE: Resolving a merger in a hyper-luminous submillimeter galaxy at z=2.82
AUTHOR: Perry, R. W., Chapman, S. C., Smail, I., Bertoldi, F.
PUBLICATION: *arXiv e-prints, arXiv:2210.08191*
PUBLICATION DATE: Oct-22
ABSTRACT: https://ui.adsabs.harvard.edu/abs/2022arXiv221008191P

TITLE: Multi-messenger characterization of Mrk 501 during historically low X-ray and γ-ray activity
AUTHOR: Abe, H., Abe, S., Acciari, V. A., Agudo, I., Aniello, T., Ansoldi, S., Antonelli, L. A., Arbet Engels, A., Arcaro, C., Artero, M., Asano, K., Baack, D., Babić, A., Baquero, A., Barres de Almeida, U., Barrio, J. A., Batković, I., Baxter, J., Becerra González, J., Bednarek, W., Bernardini, E., Bernardos, M., Berti, A., Besenrieder, J., Bhattacharyya, W., Bigongiari, C., Biland, A., Blanch, O., Bonnoli, G., Bošnjak, Ž., Burelli, I., Busetto, G., Carosi, R., Carretero-Castrillo, M., Castro-Tirado, A. J., Ceribella, G., Chai, Y., Chilingarian, A., Cikota, S., Colombo, E., Contreras, J. L., Cortina, J., Covino, S., D'Amico, G., D'Elia, V., Da Vela, P., Dazzi, F., De Angelis, A., De Lotto, B., Del Popolo, A., Delfino, M., Delgado, J., Delgado Mendez, C., Depaoli, D., Di Pierro, F., Di Venere, L., Do Souto Espiñeira, E., Dominis Prester, D., Donini, A., Dorner, D., Doro, M., Elsaesser, D., Emery, G., Escudero, J., Fallah Ramazani, V., Fariña, L., Fattorini, A., Foffano, L., Font, L., Fruck, C., Fukami, S., Fukazawa, Y., García López, R. J., Garczarczyk, M., Gasparyan, S., Gaug, M., Giesbrecht Paiva, J. G., Giglietto, N., Giordano, F., Gliwny, P., Godinović, N., Grau, R., Green, D., Green, J. G., Hadasch, D., Hahn, A., Hassan, T., Heckmann, L., Herrera, J., Hrupec, D., Hütten, M., Imazawa, R., Inada, T., Iotov, R., Ishio, K., Jiménez Martínez, I., Jormanainen, J., Kerszberg, D., Kobayashi, Y., Kubo, H., Kushida, J., Lamastra, A., Lelas, D., Leone, F., Lindfors, E., Linhoff, L., Lombardi, S., Longo, F., López-Coto, R., López-Moya, M., López-Oramas, A., Loporchio, S., Lorini, A., Lyard, E., Machado de Oliveira Fraga, B., Majumdar, P., Makariev, M., Maneva, G., Mang, N., Manganaro, M., Mangano, S., Mannheim, K., Mariotti, M., Martínez, M., Mas-Aguilar, A., Mazin, D., Menchiari, S., Mender, S., Mićanović, S., Miceli, D., Miener, T., Miranda, J. M., Mirzoyan, R., Molina, E., Mondal, H. A., Moralejo, A., Morcuende, D., Moreno, V., Nakamori, T., Nanci, C., Nava, L., Neustroev, V., Nievas Rosillo, M., Nigro, C., Nilsson, K., Nishijima, K., Njoh Ekoume, T., Noda, K., Nozaki, S., Ohtani, Y., Oka, T., Okumura, A., Otero-Santos, J., Paiano, S., Palatiello, M., Paneque, D., Paoletti, R., Paredes, J. M., Pavletić, L., Persic, M., Pihet, M., Pirola, G., Podobnik, F., Prada Moroni, P. G., Prandini, E., Principe, G., Priyadarshi, C., Rhode, W., Ribó, M., Rico, J., Righi, C., Rugliancich, A., Sahakyan, N., Saito, T., Sakurai, S., Satalecka, K., Saturni, F. G., Schleicher, B., Schmidt, K., Schmuckermaier, F., Schubert, J. L., Schweizer, T., Sitarek, J., Sliusar, V., Sobczynska, D., Spolon, A., Stamerra, A., Strišković, J., Strom, D., Strzys, M., Suda, Y., Surić, T., Tajima, H., Takahashi, M., Takeishi, R., Tavecchio, F., Temnikov, P., Terauchi, K., Terzić, T., Teshima, M., Tosti, L., Truzzi, S., Tutone, A., Ubach, S., van Scherpenberg, J., Vazquez Acosta, M., Ventura, S., Verguilov, V., Viale, I., Vigorito, C. F., Vitale, V., Vovk, I., Walter, R., Will, M., Wunderlich, C., Yamamoto, T., Zarić, D., Other groups, collaborations, :, Cerruti, M., Acosta-Pulido, J. A., Apolonio, G., Bachev, R., Baloković, M., Benítez, E., Björklund, I., Bozhilov, V., Brown, L. F., Bugg, A., Carbonell, W., Carnerero, M. I., Carosati, D., Casadio, C., Chamani, W., Chen, W. P., Chigladze, R. A., Damljanovic, G., Epps, K., Erkenov, A., Feige, M., Finke, J., Fuentes, A., Gazeas, K., Giroletti, M., Grishina, T. S., Gupta, A. C., Gurwell, M. A., Heidemann, E., Hiriart, D., Hou, W. J., Hovatta, T., Ibryamov, S., Joner, M. D., Jorstad, S. G., Kania, J., Kiehlmann, S., Kimeridze, G. N., Kopatskaya, E. N., Kopp, M., Korte, M., Kotas, B., Koyama, S., Kramer, J. A., Kunkel, L., Kurtanidze, S. O., Kurtanidze, O. M., Lähteenmäki, A., López, J. M., Larionov, V. M., Larionova, E. G., Larionova, L. V., Leto, C., Lorey, C., Mújica, R., Madejski, G. M., Marchili, N., Marscher, A. P., Minev, M., Modaressi, A., Morozova, D. A., Mufakharov, T., Myserlis, I., Nikiforova, A. A., Nikolashvili, M. G., Ovcharov, E., Perri, M., Raiteri, C. M., Readhead, A. C. S., Reimer, A., Reinhart, D., Righini, S., Rosenlehner, K., Sadun, A. C., Savchenko, S. S., Scherbantin, A., Schneider, L., Schoch, K., Seifert, D., Semkov, E., Sigua, L. A., Singh, C., Sola, P., Sotnikova, Y., Spencer, M., Steineke, R., Stojanovic, M., Strigachev, A., Tornikoski, M., Traianou, E., Tramacere, A., Troitskaya, Y. V., Troitskiy, I. S., Trump, J. B., Tsai, A., Valcheva, A., Vasilyev, A. A., Verrecchia, F., Villata, M., Vince, O., Vrontaki, K., Weaver, Z. R., Zaharieva, E., Zottmann, N.
PUBLICATION: *arXiv e-prints, arXiv:2210.02547*
PUBLICATION DATE: Oct-22
ABSTRACT: https://ui.adsabs.harvard.edu/abs/2022arXiv221002547A

TITLE: CN 2-1 and CS 5-4 Observations toward Arp 299 with the SMA
AUTHOR: Wang, J., Qi, C., Li, S., Wu, J.
PUBLICATION: *The Astrophysical Journal, 937, 120*
PUBLICATION DATE: Oct-22
ABSTRACT: https://ui.adsabs.harvard.edu/abs/2022ApJ...937..120W
DOI: 10.3847/1538-4357/ac9122

TITLE: Mapping NGC 7027 in New Light: CO^+ and HCO^+ Emission Reveal Its Photon- and X-ray-Dominated Regions
AUTHOR: Bublitz, J., Kastner, J. H., Hily-Blant, P., Forveille, T., Santander-Garc√≠a, M., Alcolea, J., Bujarrabal, V., Wilner, D. J., Montez, R., Aleman, I.
PUBLICATION: *arXiv e-prints, arXiv:2209.13680*
PUBLICATION DATE: Sep-22
ABSTRACT: https://ui.adsabs.harvard.edu/abs/2022arXiv220913680B

TITLE: Accretion Burst Echoes as Probes of Protostellar Environments and Episodic Mass Assembly
AUTHOR: Francis, L., Johnstone, D., Lee, J.-E., Herczeg, G. J., Long, F., Mairs, S., Contreras Peña, C., Moriarty-Schieven, G., JCMT Transient Team
PUBLICATION: *The Astrophysical Journal, 937, 29*
PUBLICATION DATE: Sep-22
ABSTRACT: https://ui.adsabs.harvard.edu/abs/2022ApJ...937...29F
DOI: 10.3847/1538-4357/ac8a9e

TITLE: Jet kinematics in the transversely stratified jet of 3C 84. A two-decade overview
AUTHOR: Paraschos, G. F., Krichbaum, T. P., Kim, J.-Y., Hodgson, J. A., Oh, J., Ros, E., Zensus, J. A., Marscher, A. P., Jorstad, S. G., Gurwell, M. A., Lähteenmäki, A., Tornikoski, M., Kiehlmann, S., Readhead, A. C. S.
PUBLICATION: *Astronomy and Astrophysics, 665, A1*
PUBLICATION DATE: Sep-22
ABSTRACT: https://ui.adsabs.harvard.edu/abs/2022A&A...665A...1P
DOI: 10.1051/0004-6361/202243343

TITLE: Resolving the Inner Parsec of the Blazar J1924-2914 with the Event Horizon Telescope
AUTHOR: Issaoun, S., Wielgus, M., Jorstad, S., Krichbaum, T. P., Blackburn, L., Janssen, M., Chan, C.-. kwan ., Pesce, D. W., Gómez, J. L., Akiyama, K., Mościbrodzka, M., Martí-Vidal, I., Chael, A., Lico, R., Liu, J., Ramakrishnan, V., Lisakov, M., Fuentes, A., Zhao, G.-Y., Moriyama, K., Broderick, A. E., Tiede, P., MacDonald, N. R., Mizuno, Y., Traianou, E., Loinard, L., Davelaar, J., Gurwell, M., Lu, R.-S., Alberdi, A., Alef, W., Algaba, J. C., Anantua, R., Asada, K., Azulay, R., Bach, U., Baczko, A.-K., Ball, D., Baloković, M., Barrett, J., Bauböck, M., Benson, B. A., Bintley, D., Blundell, R., Boland, W., Bouman, K. L., Bower, G. C., Boyce, H., Bremer, M., Brinkerink, C. D., Brissenden, R., Britzen, S., Broguiere, D., Bronzwaer, T., Bustamante, S., Byun, D.-Y., Carlstrom, J. E., Ceccobello, C., Chatterjee, K., Chatterjee, S., Chen, M.-T., Chen, Y., Cho, I., Christian, P., Conroy, N. S., Conway, J. E., Cordes, J. M., Crawford, T. M., Crew, G. B., Cruz-Osorio, A., Cui, Y., Laurentis, M. D., Deane, R., Dempsey, J., Desvignes, G., Dexter, J., Doeleman, S. S., Dhruv, V., Dzib Quijano, S. A., Eatough, R. P., Emami, R., Falcke, H., Farah, J., Fish, V. L., Fomalont, E., Ford, H. A., Fraga-Encinas, R., Freeman, W. T., Friberg, P., Fromm, C. M., Galison, P., Gammie, C. F., García, R., Gentaz, O., Georgiev, B., Goddi, C., Gold, R., Gómez-Ruiz, A. I., Gu, M., Hada, K., Haggard, D., Hecht, M. H., Hesper, R., Ho, L. C., Ho, P., Honma, M., Huang, C.-W. L., Huang, L., Hughes, D. H., Ikeda, S., Impellizzeri, C. M. V., Inoue, M., James, D. J., Jannuzi, B. T., Jeter, B., Jiang, W., Jimenez-Rosales, A., Johnson, M. D., Joshi, A. V., Jung, T., Karami, M., Karuppusamy, R., Kawashima, T., Keating, G. K., Kettenis, M., Kim, D.-J., Kim, J.-Y., Kim, J., Kim, J., Kino, M., Koay, J. Y., Kocherlakota, P., Kofuji, Y., Koch, P. M., Koyama, S., Kramer, C., Kramer, M., Kuo, C.-Y., Bella, N. L., Lauer, T. R., Lee, D., Lee, S.-S., Leung, P. K., Levis, A., Li, Z., Lico, R., Lindahl, G., Lindqvist, M., Liu, K., Liuzzo, E., Lo, W.-P., Lobanov, A. P., Lonsdale, C., Mao, J., Marchili, N., Markoff, S., Marrone, D. P., Marscher, A. P., Matsushita, S., Matthews, L. D., Medeiros, L., Menten, K. M., Michalik, D., Mizuno, I., Mizuno, Y., Moran, J. M., Müller, C., Mus, A., Musoke, G., Myserlis, I., Nadolski, A., Nagai, H., Nagar, N. M., Nakamura, M., Narayan, R., Narayanan, G., Natarajan, I., Nathanail, A., Neilsen, J., Neri, R., Ni, C., Noutsos, A., Nowak, M. A., Oh, J., Okino, H., Olivares, H., Ortiz-León, G. N., Oyama, T., Özel, F., Palumbo, D. C. M.,

Paraschos, G. F., Park, J., Parsons, H., Patel, N., Pen, U.-L., Piétu, V., Plambeck, R., PopStefanija, A., Porth, O., Pötzl, F. M., Prather, B., Preciado-López, J. A., Psaltis, D., Pu, H.-Y., Rao, R., Rawlings, M. G., Raymond, A. W., Rezzolla, L., Ricarte, A., Ripperda, B., Roelofs, F., Rogers, A., Ros, E., Romero-Canizales, C., Roshanineshat, A., Rottmann, H., Roy, A. L., Ruiz, I., Ruszczyk, C., Rygl, K. L. J., Sánchez, S., Sánchez-Arguelles, D., Sanchez-Portal, M., Sasada, M., Satapathy, K., Savolainen, T., Schloerb, F. P., Schuster, K.-F., Shao, L., Shen, Z., Small, D., Sohn, B. W., SooHoo, J., Souccar, K., Sun, H., Tazaki, F., Tetarenko, A. J., Tiede, P., Tilanus, R. P. J., Titus, M., Torne, P., Trent, T., Trippe, S., van Bemmel, I., van Langevelde, H. J., van Rossum, D. R., Vos, J., Wagner, J., Ward-Thompson, D., Wardle, J., Weintroub, J., Wex, N., Wharton, R., Wiik, K., Witzel, G., Wondrak, M., Wong, G. N., Wu, Q., Yamaguchi, P., Yoon, D., Young, A., Young, K., Younsi, Z., Yuan, F., Yuan, Y.-F., Zensus, J. A., Zhang, S., Zhao, S.-S.

PUBLICATION: *The Astrophysical Journal, 934, 145*
PUBLICATION DATE: Aug-22
ABSTRACT: https://ui.adsabs.harvard.edu/abs/2022ApJ...934..145I
DOI: 10.3847/1538-4357/ac7a40

TITLE: Luminous Millimeter, Radio, and X-Ray Emission from ZTF 20acigmel (AT 2020xnd)
AUTHOR: Ho, A. Y. Q., Margalit, B., Bremer, M., Perley, D. A., Yao, Y., Dobie, D., Kaplan, D. L., O
PUBLICATION: *The Astrophysical Journal, 932, 116*
PUBLICATION DATE: Jun-22
ABSTRACT: https://ui.adsabs.harvard.edu/abs/2022ApJ...932..116H
DOI: 10.3847/1538-4357/ac4e97

TITLE: The methanol emission in the J1- J0 A-+ line series as a tracer of specific physical conditions in high-mass star-forming regions
AUTHOR: Salii, S. V., Zinchenko, I. I., Liu, S.-Y., Sobolev, A. M., Aberfelds, A., Su, Y.-N.
PUBLICATION: *Monthly Notices of the Royal Astronomical Society, 512, 3215-3229*
PUBLICATION DATE: May-22
ABSTRACT: https://ui.adsabs.harvard.edu/abs/2022MNRAS.512.3215S
DOI: 10.1093/mnras/stac739

TITLE: A Multiwavelength Study of ELAN Environments (AMUSE2). Mass Budget, Satellites Spin Alignment, and Gas Infall in a Massive z 3 Quasar Host Halo
AUTHOR: Arrigoni Battaia, F., Chen, C.-C., Liu, H.-Y. B., De Breuck, C., Galametz, M., Fumagalli, M., Yang, Y., Zanella, A., Man, A., Obreja, A., Prochaska, J. X., Bañados, E., Hennawi, J. F., Farina, E. P., Zwaan, M. A., Decarli, R., Lusso, E.
PUBLICATION: *The Astrophysical Journal, 930, 72*
PUBLICATION DATE: May-22
ABSTRACT: https://ui.adsabs.harvard.edu/abs/2022ApJ...930...72A
DOI: 10.3847/1538-4357/ac5a4d

TITLE: Effects of Magnetic Field Orientations in Dense Cores on Gas Kinematics in Protostellar Envelopes
AUTHOR: Gupta, A., Yen, H.-W., Koch, P., Bastien, P., Bourke, T. L., Chung, E. J., Hasegawa, T., Hull, C. L. H., Inutsuka, S.-. ichiro ., Kwon, J., Kwon, W., Lai, S.-P., Lee, C. W., Lee, C.-F., Pattle, K., Qiu, K., Tahani, M., Tamura, M., Ward-Thompson, D.
PUBLICATION: *The Astrophysical Journal, 930, 67*
PUBLICATION DATE: May-22
ABSTRACT: https://ui.adsabs.harvard.edu/abs/2022ApJ...930...67G
DOI: 10.3847/1538-4357/ac63bc

TITLE: Massive Molecular Gas Reservoir in a Luminous Submillimeter Galaxy during Cosmic Noon

AUTHOR: Liu, B., Chartab, N., Nayyeri, H., Cooray, A., Yang, C., Riechers, D. A., Gurwell, M., Zhu, Z.-. hong ., Serjeant, S., Borsato, E., Negrello, M., Marchetti, L., Corsini, E. M., van der Werf, P.

PUBLICATION: *The Astrophysical Journal, 929, 41*

PUBLICATION DATE: Apr-22

ABSTRACT: https://ui.adsabs.harvard.edu/abs/2022ApJ...929...41L

DOI: 10.3847/1538-4357/ac5745

TITLE: Virial Clumps in Central Molecular Zone Clouds

AUTHOR: Myers, P. C., Hatchfield, H. P., Battersby, C.

PUBLICATION: *The Astrophysical Journal, 929, 34*

PUBLICATION DATE: Apr-22

ABSTRACT: https://ui.adsabs.harvard.edu/abs/2022ApJ...929...34M

DOI: 10.3847/1538-4357/ac5906

Photo by Brooks Rownd

The Submillimeter Array (SMA) is a pioneering radio-interferometer dedicated to a broad range of astronomical studies including finding protostellar disks and outflows; evolved stars; the Galactic Center and AGN; normal and luminous galaxies; and the solar system. Located on Maunakea, Hawaii, the SMA is a collaboration between the Smithsonian Astrophysical Observatory and the Academia Sinica Institute of Astronomy and Astrophysics.